Structural design of gallium oxide devices toward practical applications

（実用化に向けた酸化ガリウムデバイスの構造設計）

51427355

RAMA VENKATA KRISHNA RAO

Division of Industrial Innovation Sciences

Graduate School of Natural Science and Technology

OKAYAMA UNIVERSITY

This dissertation is submitted for the degree of Doctor of Engineering

2022, March

DECLARATION

The material presented in this thesis is the outcome of my research under the supervision of Professor Yasuhiko HAYASHI at Okayama University. It has not been previously submitted, in part or whole, to any university or institution for any degree or other qualification.

Signed:

Name: RAMA VENKATA KRISHNA RAO

Date: 17th February 2022

Structural design of gallium oxide devices toward practical applications

Abstract

This thesis mainly discussed achieving two significant areas on synthesizing comprehensive bandgap semiconductor materials and fabricating ultraviolet photoresponsive devices. At the beginning of this research work, the self-assembled fullerene (C_{60}) was explored by the liquid-liquid interface precipitation (LLIP) technique. Further, the gallium oxide (Ga_2O_3) wide bandgap semiconductor is ·studied to fabricate heterojunction devices, considering its excellent electronic, mechanical, and chemical properties. Wide bandgap semiconductors like Gallium Nitride (GaN) and Ga_2O_3 which possess a bandgap of 3.4 eV and 4.5-4.9 eV, respectively, have attracted significant interest for ultraviolet and deep ultraviolet photoresponsive device applications. Thus, integrating these wide bandgaps and ultra-wide bandgap semiconductors with inorganic compound semiconductors like copper iodide (γ-CuI) to fabricate Schottky and p-n heterojunctions is an exciting prospect for optoelectronics. In this regard, the present thesis investigates the fabrication of γ-CuI with Ga_2O_3 to form heterojunction optoelectronic devices, followed by an investigation of the quality of heterojunction interface for solar-blind UV photodetector application. The temperature-dependent studies also investigated the γ-CuI and Ga_2O_3-based heterojunction devices to understand the device properties.

Further, the Schottky junction properties of gallium oxide (Ga_2O_3) were investigated with an interfacial hexagonal boron nitride (hBN) layer. A chemical vapour-deposited hBN film was transferred on the Ga_2O_3 substrate, and a vertical Schottky junction was fabricated with Ni/h-BN/Ga_2O_3/In configuration. The current-voltage characteristics of the Schottky junction area are investigated by comparing with and without the hBN interfacial layer. It is shown that the turn-on voltage for the forward current of the Schottky junction was significantly enhanced with

the h-BN interfacial film. Further, the Schottky junction was analyzed under deep ultraviolet light (254 nm) illumination, significant photoresponsivity of 95.11 mA/W under an applied bias voltage (-8 V). The interfacial layer of hBN for the Ga_2O_3-based Schottky junction can be substantial as a barrier layer to control the turn-on voltage and optimize the device properties for deep UV photosensor applications. The above studies clarify the synthesis of comprehensive bandgap semiconductor materials such as fullerene Nanorods, hBN layer ·, and γ-CuI film, and fabrication of γ-CuI/Ga_2O_3 and Ni/h-BN/Ga_2O_3 heterojunction devices.

Thesis Outline

Chapter 1

This thesis mainly discussed achieving the Structural design of gallium oxide devices toward practical applications Wide bandgap semiconductors like Gallium Nitride (GaN) and Ga_2O_3 possess a bandgap of 3.4 eV and 4.5-4.9 eV, respectively, have attracted significant interest for ultraviolet and deep ultraviolet photoresponsive device applications. Thus, integrating these wide bandgaps and ultra-wide bandgap semiconductors with inorganic compound semiconductors like copper iodide (γ-CuI) to fabricate Schottky and p-n heterojunctions is an exciting prospect for optoelectronics. In this regard, the present thesis investigates the fabrication of γ-CuI with Ga_2O_3 to form heterojunction optoelectronic devices, followed by an investigation of the quality of heterojunction interface for solar-blind UV photodetector application. The temperature-dependent studies also investigated the γ-CuI and Ga_2O_3-based heterojunction devices to understand the device properties. Further, The Schottky junction properties of gallium oxide (Ga_2O_3) were analyzed with an interfacial hexagonal boron nitride (hBN) layer. Thereby revealing their interface properties at various temperatures. CuI is an environmentally-friendly material composed of non-toxic and naturally abundant elements. Present in seawater, iodine is the heaviest essential element. (CuI) has been considered as a promising inorganic p-type semiconductor material in its applications.

Chapter 2

Engineered carbon-based nanomaterials are being used in biomedical applications, such as drug-delivery systems, cancer therapy, and electronic devices. It is widely known that buckminsterfullerene, or fullerene (C_{60}), is a truncated icosahedron formed by sp^2 hybridized carbon atoms. Its peculiar external shape is due to 20 hexagons and 12 pentagons. Allotropic forms of carbon show significant properties, such as opt, electrical, optoelectronic, and

redox properties; effective n-doping of organic semiconductors; and high conductivity, making them one of the most promising elements in chemistry. Self-assembled nanostructures show electron-transfer improvements when compared with planar electron acceptors. This property allows the development of organic electron devices (e.g., field-effect transistors and solar cells) and optoelectronic devices. Nanotechnology is an emerging field of growing importance. The driving force behind the search for Nano-sized materials is the continuing demand for minimization in electronic devices' dimensions while optimizing their performance. With the reduction in size and shape, these materials exhibit unique optoelectronic properties, size-dependent in contrast to their corresponding bulk materials.

Chapter 3 Here, another exciting material is Ga_2O_3 gallium oxide temperature-dependent studies of Ga_2O_3 based heterojunction devices are essential in understanding its carrier transport mechanism, junction barrier potential, and stability at higher temperatures. In this study, we investigated the temperature-dependent device characteristics of the p-type γ-copper iodide (γ-CuI)/n-type β-gallium oxide (β-Ga_2O_3) heterojunctions, thereby revealing their interface properties. The fabricated γ-CuI/β-Ga_2O_3 heterojunction showed excellent diode characteristics with a high rectification ratio and low reverse saturation current at 298 K in a significant barrier height (0.632 eV). To investigate the heterojunction interface, the temperature-dependent device characteristics were studied in the 273 – 473 K temperature range. With an increase in temperature, a gradual decrease in the ideality factor and an increase in the barrier height were observed, indicating barrier inhomogeneity at the heterojunction interface. Furthermore, the current-voltage measurement showed electrical hysteresis for the reverse saturation current, although it was not observed for the forward bias current. The presence of electrical hysteresis for the reverse saturation current and the barrier inhomogeneity in the temperature-dependent characteristics indicates some level of interface states for the γ-CuI/ β-Ga_2O_3 heterojunction device. Thus, our study showed that

electrical hysteresis could be correlated with temperature-dependent electrical features of the β-Ga$_2$O$_3$-based heterojunction device, which signifies the presence of surface defects and interface states.

Chapter 4 By Investing the device properties for a nickel (Ni)-gallium oxide (Ga$_2$O$_3$) Schottky junction with the interfacial hexagonal boron nitride (hBN) layer. Chemical vapour deposited hBN film was transferred onto the Ga$_2$O$_3$ substrate, and a vertical Schottky junction was fabricated with the Ni/hBN/Ga$_2$O$_3$/In configuration. The current-voltage characteristics of the Schottky junction were investigated by comparing with and without the hBN interfacial layer. We observed that the turn voltage for the forward current of the Schottky junction was significantly enhanced with the hBN interfacial film. Further, the Schottky junction was analyzed under deep ultraviolet light (254 nm), obtaining a photoresponsivity of 95.11 mA/W under an applied bias voltage (-8 V). The interfacial layer of hBN for the Ga$_2$O$_3$-based Schottky junction can be significant as a barrier layer to control the turn-on voltage and optimize the device properties for deep UV photosensor applications. Further, the demonstrated vertical heterojunction with an hBN layer can be obtained for temperature management at the junction interface to develop reliable Ga$_2$O$_3$-based Schottky junction devices. Finally, the effort of this research will significantly contribute to practical applications for self-powered, low power consuming transistor applications.

Chapter 5 Wide bandgap and ultrawide bandgap semiconductors like temperature-dependent device characteristics of the p-type γ-copper iodide (γ-CuI)/n-type β-gallium oxide (β-Ga$_2$O$_3$) attractive candidates for UV and deep UV photodetector application. In this research work, integration of γ-CuI and (β-Ga$_2$O$_3$) heterojunctions with 2-dimensional hBN, and novel inorganic wide bandgap semiconductor, i.e., CuI, is studied. Further, the device performance of Ni/hBN/Ga$_2$O$_3$/In is evaluated concerning interfacial impurities under UV light illumination.

Table of Contents

ABBREVIATIONS

FNCT   Fullerene Nano cylindrical Tubes

LLIP   Liquid-liquid interface precipitation

TAB   Tetra butyl alcoholic

FE-SEM   Field emission scanning electron microscopy

HR-TEM   High-resolution transmission electron microscopy

FT-IT   Fourier-transform infrared spectroscopy

XRD   X-ray diffraction

CVD   Chemical vapour deposition

TFT   Thin film transistors

List of Figures:

List of Tables

CHAPTER 1

Introduction

1.1 Research Background

1.1.1 Fullerene nanostructures

Fullerenes and fullerene-related molecules structures have attracted much attention since their discovery at the laboratory (Kroto et al. 1985) [1] due to their potential applications in technology research. Fullerene nanostructured materials exhibit the combined properties of both fullerene and nanostructures, highly resistant and stable tridimensional molecules in medicine, such as drug delivery, environmental remediation, and energy and electronics formed exclusively by 60 or more carbon atoms with the attention of excellent optoelectronic features, modified band edges, high electron affinity, fast charge transfer capabilities, and tunable structural and textural properties. These magnetic properties allow their utilization in many applications such as polymer solar cells, photovoltaics, photocatalysis, photodynamic therapy, electrocatalysis, environmental remediation, and drug and gene delivery. The supramolecular self-assembly and functionalization of fullerenes through robust chemistry approaches such as surface oxidation, grafting, polymer coating, doping of metals/nonmetal heteroatoms, noncovalent modification with 2D materials, and nanoparticle attachment result in achieving fine control over its surface and bulk properties, including increased solubility, wettability, electron transport, acid-base properties, adsorption, electronic conductivity, and light absorption. Numerous synthesis methods and anchoring groups are employed for functionalized fullerenes with nanostructures using convergent bottom-up and top-down strategies [3].
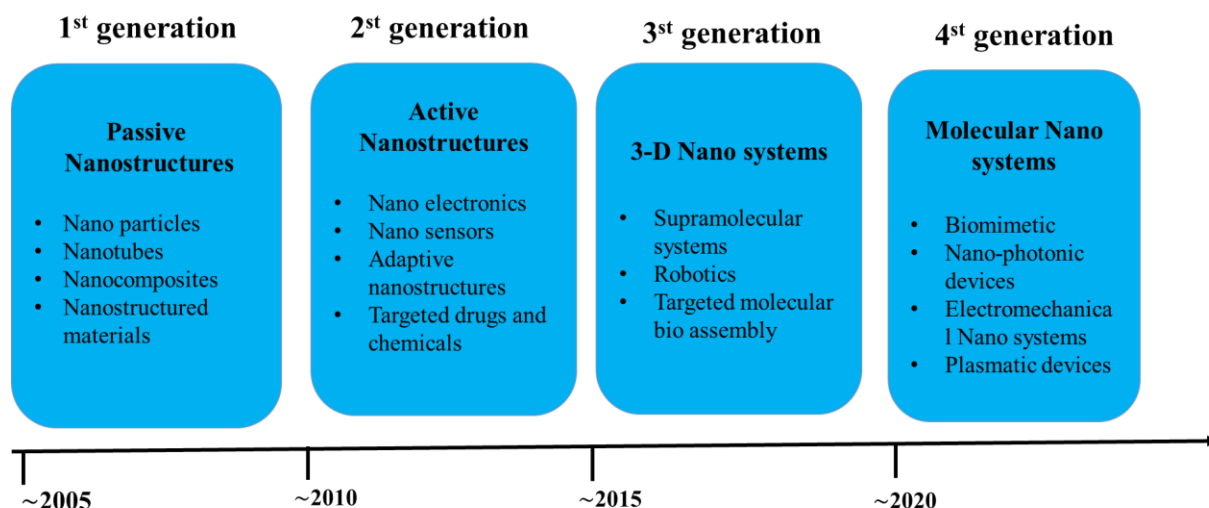
Figure1.1: Generation of nanostructures.

First-generation nanostructures show the coatings, dispersion of nanoparticles, and nanostructured materials such as metals, polymers, and ceramics. As shown in the above **Figure1.1**, the second generation represented by active nanostructures refers to adaptive nanostructures, transistors, amplifiers, targeted drugs and chemicals, and actuators. The third-generation 3D nano systems have various synthesis and assembling techniques, such as bio assembling networking at the nanoscale and multiscale architectures [4]. Here the fourth generation, the research focus will be on atomic manipulation for the design of molecules and supramolecular systems, molecular machines, and large heterogeneous molecular systems creating multifunctional molecules catalysts for synthesis, electromechanical Nano systems, subcellular interventions, and biomimetic for complex system dynamics and control.

1.1.2 C_{60} Fullerene

One of the best and most practiced methods to obtain nanostructures using fullerene is the LLIP (liquid-liquid-interface-precipitation) method. Many types of particles have been reported using this technique which stands to be very precise and effective in obtaining nanostructures. Hence we have focused in this review to bring out the insights in the LLIP mentioned above method. Most

of the examples discussed below are the recently reported LLIP methods of obtaining nanostructures. Few other techniques have also been discussed to give a fair idea about the possibilities of fullerene-based self-assembly [5].
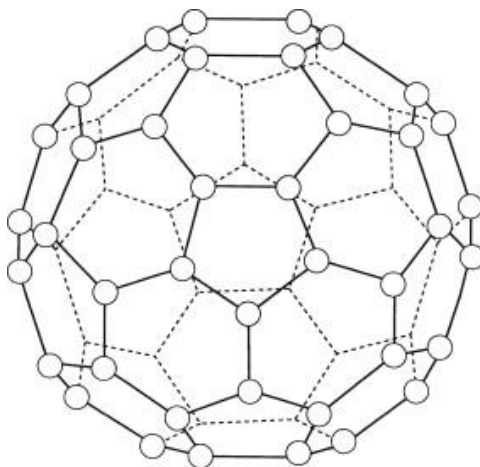
Figure 1.2: Structure of the buckminsterfullerene molecule C_{60}.

The compound C_{60}, called buckminsterfullerene or fullerene for short, consists of 60 carbon atoms at the vertices of the do triacontahedron sketched in **Figure 1.2**. The term fullerene is used here for a broader class of compounds C_n with n carbon atoms, whose carbon atoms are each bonded to three other carbons to form a closed surface, with the system conjugated such that for every resonant structure, each carbon has two single bonds and one double bond [6]. The possible minor compound of this type is tetrahedral C_4, which has the three resonant structures shown in **Figure. 1.2**. These hypothetical more minor C_n compounds have not been synthesised, but the larger ones, such as C_{60}, C_{70}, C_{76}, C_{78}, and C_{82}, have been made and characterised. Some have several forms, with different arrangements of 12 pentagons and numerous hexagons. Clusters of Buckman, such as icosahedral $(C_{60})_{13}$, have also been studied [7].

The synthesis of self-assembled nanostructures using C_{60} with many solvents results in different ordered structures like Nanosheets, Nanorods, Nano fullerene whiskers, etc. Most of the C_{60}

solvates are not stable in the atmosphere. It degrades rapidly when removed from the mother liquor. The procedure for obtaining these structures has a basic approach, i.e., the process includes a saturated solution and a solvent. The saturated solution is a mixture of a solvent and fullerene of a known ratio. The formation of nanostructures is by the particle interaction, which depends on various factors such as temperature, stability, the boiling point of the solvent used in the saturated solution, etc. When the two solvents are mixed, a layer is formed in between called the interface layer. This synthesis method is known as the Liquid-Liquid interface precipitation (LLIP) method. It is a well-known fact that the LLIP method acts as nucleation sites of crystals and forms the first step of the thermodynamic phase, which helps determine the formation of crystals. This LLIP method is the most followed, most reported, and well-known method to obtain nanostructures using self-assembly fullerene [8]. The following are some of the famous and recent reports on LLIP self-assembly fullerene and her recent changes in the LLIP method. We intend to put all of the parametric modifications that lead to the successful synthesis of self-assembled fullerene nanostructures to upskill researchers with more precision and achieve their objective. Buckminsterfullerene displays different properties that render this material suitable for utilization in optoelectronic applications. The utilization of fullerene molecules in composite frameworks is incredibly encouraging. After photo-excitation, the conjugated polymer fullerene can go about as a proficient electron acceptor in a photo-induced electron exchange process. The majority of the trials as of recently have been restricted to the examination of basic mix framework where the fullerene and the polymer are blended in the same dissolvable and, after that, turn cast in a thin, stronger film. Keeping in mind the end goal to comprehend the central photo-physics in such frameworks and for a configuration of novel hetero-structures, it is essential to create strategies for treating ultrathin fullerene movies. This commitment provides details regarding the manufacture and portrayal of self-assembled nanostructures.

Self-assembly is one of the novel techniques to fabricate organic devices. Fullerenes are self-assembled by different techniques due to their advantages. Recent advancements in fullerene self-assembly have led to the invention of unaccustomed structures, which can have huge potential applications in organic devices.

The ability to engineer distinct one-, two-or three-dimensional patterns at the supra-molecular level by modifying specific chemical components is a crucial step toward nanometer-sized technology. Preliminary and successful methodologies have yielded many non-covalently bonded structures in solutions and crystals. However, the possibility of regulating the size and shape of nanostructures about function remains a current challenge of exceptional interest. It is therefore expected that the rules of Nano-patterning of organic molecules, either spontaneous or induced, once understood, can play a significant role in future and emerging technologies. Fundamental requisites, accompanying the addition of well-designed chemical functionalities to drive self-assembly processes to (pre)determined mesoscopic shapes of controlled sizes and outer-shell structures, are the conservation, and possibly even the enhancement, of the molecular level properties. To this end, fullerenes are ideal. Because of their excellent electronic properties, most of their derivatives have so far been shown to be outstanding electron acceptors and because their amphiphilic products were recently found to self-assemble at the nanometer scale to furnish Nanorods and vesicle patterns. Fullerene tends to form clusters of different sizes, especially in polar solvents. Aggregation of C_{60} units may cause a significant change in their photochemical and photophysical properties compared with isolated molecules in solution. Of course, this change can profoundly influence fullerene-based optical and electronic materials. For instance, the aggregation of fullerene spheroids was shown to play a crucial role in preparing photovoltaic cells.

The name self-assembly itself brings one an idea of a type of interaction that binds on its own to form a new compound. In other words, self-assembly is an externally unguided or unmanaged

spontaneous organization's components to create an orderly pattern. Researchers are curious and trying to understand the fundamentals of self-assembly. Once know all the theories of self-assembly, there won't be any by-product or much energy needed to synthesise complex molecules and compound materials. It's a new area of research in nanotechnology but an old phenomenon. Many nanomaterials are being synthesised self-assembly techniques example: self-assembly of metal nanostructures, self-assembly of carbon nanotubes, Nanobiology, etc., which have a more comprehensive application and more comprehension compared to the conventional synthesis techniques such as top-down, bottom-up, solution combustion, and sol-gel. Therefore, the self-assembly technique has proclaimed the interest of researchers all around the globe.

Self-assembly, in which consecutive components are molecules, is termed Molecular self-assembly. Molecular self-assembly is classified into two types intermolecular self-assembly and intramolecular self-assembly. Intermolecular self-assembly refers to the assembly or bonding between two different molecules. In contrast, intramolecular self-assembly refers to the group or bonding of two different other same elements within a molecule. As of now, it is clear that self-assembly has been happening between very tiny particles, and the key lies in the particle interaction, which leads to a successful and desired self-assembly.

Self-assembly is everywhere. The following are a few examples of self-assemblies.

Self-assembly does not only happen between molecules or atoms. It also happens between mesoscopic and macroscopic components. So self-assembly is everywhere and plays a vital role in building life.

Where does fullerene-based self-assembly have its applications?

Fullerene-based self-assembled nanostructures have been found no less than any other remarkable nanomaterials in almost all the significant fields of science and technology. It has sensors in electronics, biomedical, drug delivery, biometrics, etc. Furthermore, the self-assembly of progress is yet to be achieved and can be boomed in the industry for better support for humanity practically.

1.1.3. γ-copper iodide (γ-CuI) films

Alternative energy sources are being explored to reduce fossil fuels and pollutant emissions. Green energy sources such as thermoelectric materials converters require little maintenance. Life-time testing has shown the capability of thermoelectric devices to exceed 100,000 h of steady-state operation. On the other hand, they are used for applications with high energetic relevance that include temperature control of scientific instruments to household air-cooling systems. The current trend for developing transparent, flexible, and large-area electronics creates other challenges in thermoelectric material applications—some of the fine oxide materials and conductors of n-type present adequate properties for application in thermoelectric devices. In the case of cooling processes, these need n-type and p-type elements. For the current scarcity of existing p-type elements, copper iodide is one of those that better fulfils all requirements: transparent and p-type electrical conductive, an abundant and environmentally friendly material. In this dissertation, CuI thin films 1µm were produced through copper iodination via vapour or solid and deposited via resistive thermal evaporation of copper iodide, obtaining the γ-CuI phase in all cases. The thickness of Cu films was varied, and the influence of iodination times was studied in vapour and solid methods. A thorough analysis of the thickness effect on electrical properties was studied in samples prepared via thermal evaporation. The obtained results have shown to be possible to get films with a bandgap of ~3.02 eV holes' mobility of around 3×10^{18} cm^{-3} in films. The thickness of the CuI

layer was controlled by varying the deposition duration obtained via solid and vapour iodination. Every surface has steps, but in the prior work, the steps were on a hard-engineered vicinal surface, which means they all go down or up. But on copper (111), the steps are up and down, by just an atom or two randomly, offered by the fundamental thermodynamics.
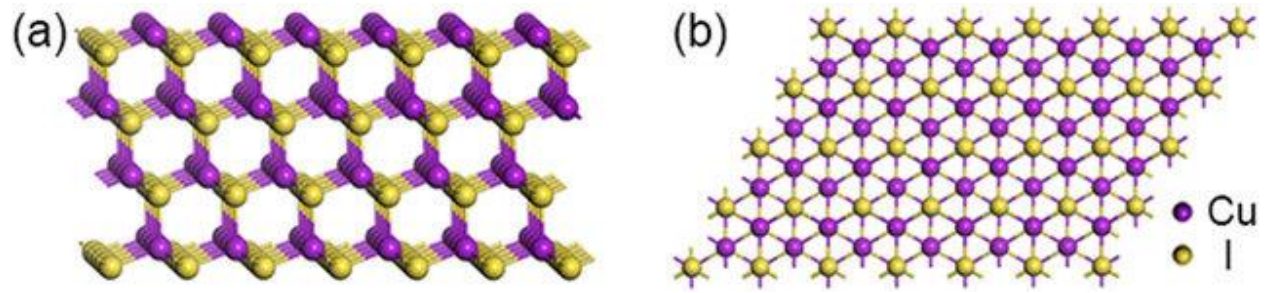
Figure 1.3: Stick-and-ball crystal structures of γ-CuI. a Side view of the cubic crystal structure of γ-CuI along the (111) plane. b Top view of γ-CuI cubic crystal above the (111) plane. [31]

Gallium oxide (Ga_2O_3) belongs to a group of ultrawide bandgap semiconductors as it possesses a bandgap of 4.5eV to 4.9eV. [9,10] The ultrawide bandgap of Gallium oxide corresponds to deep the ultraviolet region, i.e., UV-B region of the electromagnetic radiation. This invariantly separates Ga_2O_3 from other conventional wide-bandgap semiconductors like GaN and SiC. The solar-blind ultraviolet photodetectors are of great importance as they can accurately detect a weak signal of solar-blind irradiation (200-280nm) at the earth's ground level. Gallium oxide's detection range of 250-280 nm and insensitivity to visible and infrared radiation makes it a perfect candidate for deep ultraviolet region photodetector. Thus, Gallium oxide has attracted a lot of research for its possible application in power electronics, transparent electronic devices, sensing, space application. Gallium oxide is most valuable for its application as a deep UV photodetector as it is blind to wavelengths above 280nm, thus making it a solar-blind photodetector. The solar-blind ultraviolet photodetectors are of great importance as they can accurately detect a weak signal of solar-blind

20

irradiation (200-280nm) at the earth's ground level. Gallium oxide also possesses other properties such as chemical and thermal stability, thus making it a good candidate for working in harsh conditions. In this regard, Gallium oxide photodetectors have been reported fabricated using nanostructures, thin films, and a single crystal. As early as 2008, Oshima et al. have reported on the vertical Ga_2O_3 Schottky junction with a high photoresponsivity of 2.6-8.7 A/W [32]. Further, Ga_2O_3 has been studied using various device structures like metal-semiconductor-metal, Schottky barrier photodiode, p-n, n-n junction [33-34]. In this regard, the fabrication of unconventional Ga_2O_3 based photodetectors is an interesting prospect.

1.1.5 Properties of gallium oxide
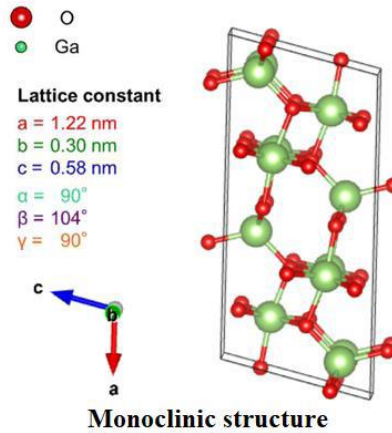
Figure 1.4: Crystal diagram of monoclinic beta- gallium oxide

Figure 1.4 shows the monoclinic structure β-Ga_2O_3 with lattice constants a= 1.22nm, b= 0.30 nm, c= 0.58nm. Gallium oxide exists in its five polymorphs, mainly α-Ga_2O_3, β-Ga_2O_3, γ-Ga_2O_3, δ-Ga_2O_3, ε-Ga_2O_3 of which the β form is the most stable polymorph in the whole temperature range. All the polymorphs transform to β-Ga_2O_3 above the temperature range 750-900 C; thus, β-Ga_2O_3 has attracted great attention than other polymorphs due to its availability [35]. However, among all the polymorphs, the β-Ga_2O_3 has poor thermal conductivity. Thermal conductivity is dependent

on the crystal direction due to crystalline anisotropy. Along the [100] plane, the thermal conductivity is 13.6 W/m/k, while along the [010] direction, it is 22.8 W/m/k. Typically the thermal conductivity of gallium oxide is about one order lesser than β-Ga_2O_3, showing a critical breakdown field of 8MV/cm, the good electron mobility of 300cm2/Vs, and high chemical stability.

1.1.6 Electronic structure
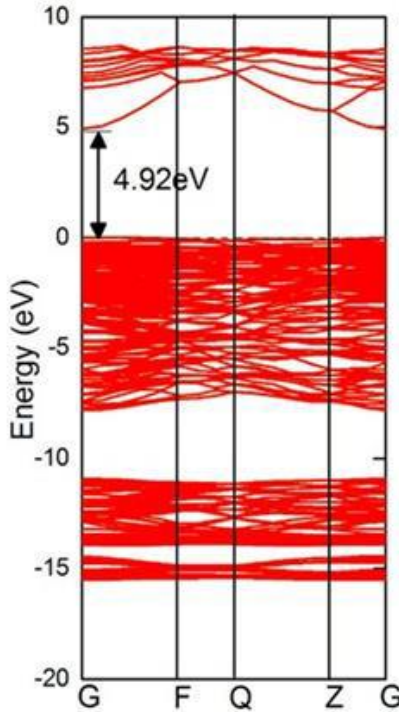
Figure 1.5 Electronic structure (D.O.S) of gallium oxide as reported by Dong et al.

Figure1.5 shows the Density of states (D.O.S) of the β-Ga_2O_3 as reported by Dong et al. [11]. The direct bandgap is observed at 4.92eV as both conduction and valence bands are situated at G point [36]. Further, the delocalised Ga 4s derived states make up the conduction band, giving the disperse band a low electron effective mass. Concurrently forming valence band occurs by hybridisation occupied O 2p6 with Ga 3d, 4p, 4s orbitals [36]. It is generally accepted that β-Ga_2O_3 has a direct bandgap in the range of 4.5 eV to 4.9 eV. This study reported a bandgap of 4.6eV for β-Ga_2O_3, which was calculated by the Tauc plot.
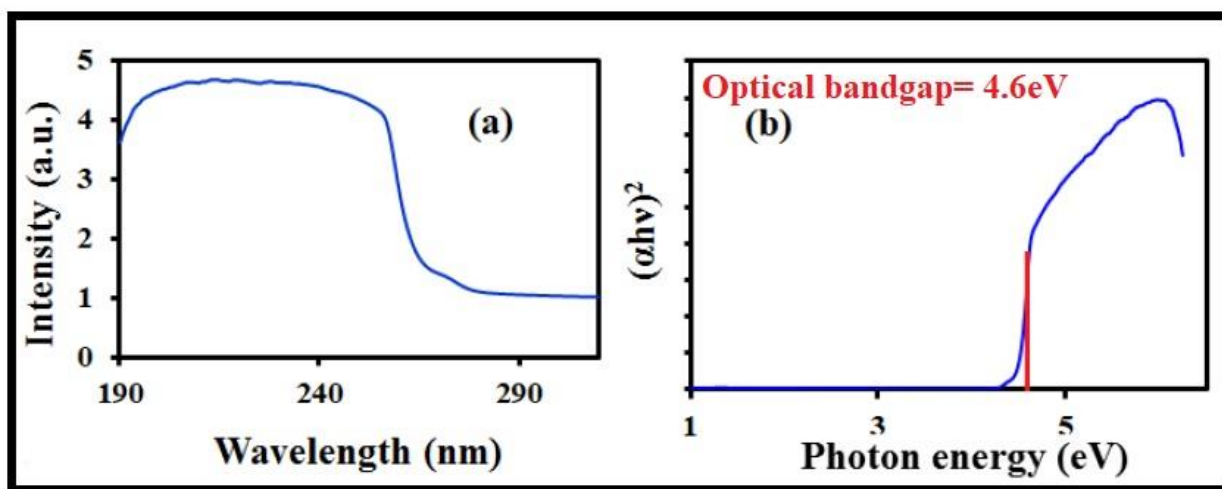
Figure 1.6: (a) The UV absorption spectra of β-Ga$_2$O$_3$ used in the present study. (b) shows the corresponding Tauc's plot to calculate the bandgap of the 4.6eV. Gallium oxide (β-Ga$_2$O$_3$), owing to its ultra-wide bandgap, is highly transparent to the UV-C region.

Figure 1.6 (a) shows the UV absorption spectra for β-Ga$_2$O$_3$ used in the present study. The absorption edge is observed in the wavelength range of 190nm – 280nm, which agrees with the theoretical values. (4.5eV- 4.9eV) This absorption can be attributed to the excitation of electrons from the valence band to the conduction band due to the overlapping of incident photon energy and the bandgap of β-Ga$_2$O$_3$. **Figure 1.6** (b) shows the Tauc plot for β-Ga$_2$O$_3$. The bandgap of the materials was calculated to be 4.53eV which agrees bandgap range 4.5eV- 4.9eV reported in the literature. Thus, β-Ga$_2$O$_3$ is completely transparent to visible and near UV irradiation, making it a solar-blind semiconductor.

1.1.7. Hexagonal boron nitride (hBN) film

Boron Nitride Films are composed of h-BN, a semiconducting insulator with a direct bandgap of 6.0 eV. Hexagonal boron nitride has been shown to have similar properties to graphene with even higher chemical stability. Single-layer h-BN and multilayer h-BN films grown on copper via

chemical vapour deposition (CVD) are available on copper foil or SiO2/Si/Ga2O3 and silicon oxide wafers. hBN is a physically and chemically stable material, making it an excellent choice for growing Ga_2O_3 films. hBN has layers that associate through der Waals interactions, which are weaker than ionic and covalent bonds, making them easier to manipulate and move. Generally, if you grow crystals of one material on another crystal, the way their atoms are arranged has to match, or the film will grow with defects.

Hexagonal boron nitride (h-BN) is an III−V compound with a structure similar to graphite and is referred to as "white graphite". It is a layered structural material with a weak van der Waals interaction between the layers. Its honeycomb structure is composed of alternating boron and nitrogen atoms within each layer instead of all carbon atoms, as in graphene.[12] While graphene/graphite is metallic/ semi-metallic in terms of its electrical properties, h-BN is an insulator with a direct bandgap (5.97 eV).2 Because of strong covalent sp2 bonds in the plane, the in-plane mechanical strength and thermal conductivity of h-BN has been reported to be close to that of graphene, whereas h-BN has even higher chemical stability than graphene; it can be stable in the air up to 1000 °C (in contrast, for graphene the corresponding temperature is ∼600 °C).[13-16] Like graphene, h-BN has a wide range of applications based on its remarkable properties, such as deep ultraviolet emitter, transparent membrane, the dielectric layer, or protective coatings.[13-17] Recently, it has been highlighted that the on-substrate mobility of graphene on exfoliated single-crystalline h-BN is comparable to that of suspended graphene due to ultra-flat flat and charge impurity-free surface. [18] The giant flex electric effect was also predicted for monolayer h-BN, suggesting its ambient agitation energy harvesting potential

It is also colloquially called "graphene's sister" since it has a similar hexagonal lattice with a modest lattice mismatch of 1.7% **Figure 1.7** (a); its hexagonal structure has been identified using

X-ray and electron diffraction. An example of the electron diffraction pattern of hBN is shown in **Figure 1.7** (b).
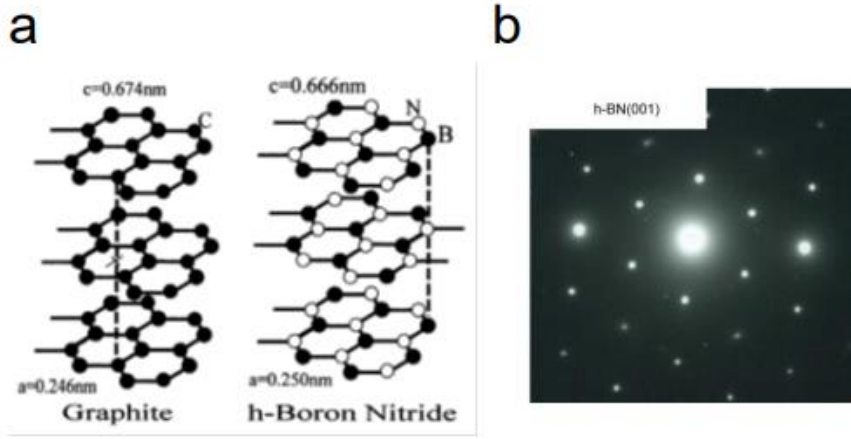
Figure 1.7: a) Schematic diagrams of crystal structures of graphite and h-BN, taken from [20]. (b) TEM electron diffraction patterns of pristine hBN, taken from [21].

Contrary to graphene, hBN is an insulator with dielectric properties similar to SiO2. Its band gap was measured to be 6 eV [22]. Therefore, it often serves as an atomic flat insulating substrate or a tunneling dielectric barrier in graphene and other 2D electronics [23,24,]. It is chemically inert in acids, solvents, and oxidizers [26]. Due to the solid covalent sp2 B-N bonds, hBN has high thermal and chemical stability, high mechanical strength, and thermal conductivity [27]. Hence, it is an attractive material for a chemically inert coating in hazardous environments.

1.2 Research Background for devices

1.2.1   Schottky Junction devices

Schottky diode is a Metal semiconductor junction diode with less forward voltage drop than the p-n junction diode and can be used in high-speed switching applications. In Schottky, diode metal such as aluminum or platinum can replace p-type semiconductors. The Schottky diode is named a

germen physicist Walter H. Schottky [28]. Schottky diode, also known as Schottky barrier diode and surface barrier diode, majority carrier device, hot-electron diode, hot carrier diode Schottky diode are widely used in radio frequency applications when aluminum or platinum metal is joined with an N-type semiconductor, a junction between the metal and n-type semiconductor. This junction is known as the metal-semiconductor junction or M-S junction.
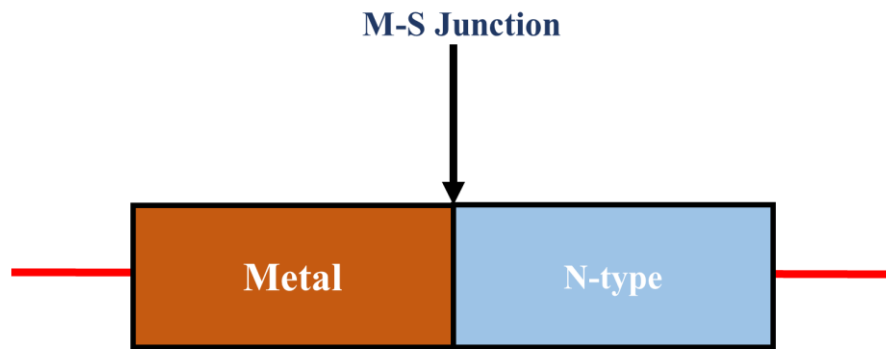
Figure 1.8: Schematic of Metal Semiconductor Junction.

A metal-semiconductor junction formed between a metal and n-type semiconductor creates a barrier or depletion layer known as the Schottky barrier. Metal – semiconductor contacts are the most crucial component in the structure of the semiconductor devices to be connected with the outside world. Two types of metal-semiconductor junctions are often present in each semiconductor device and are involved in the fabrication of solid-state devices. The first type is the rectifying contact, known as Schottky contact, and the second type is the non-rectifying contact known as Ohmic contact. The rectifying or Schottky junction allows current flow in one biasing direction and blocks current in the opposite direction. This implies tremendous resistance to current flow in the blocking order.

On the other hand, the Ohmic contact has low resistance, allowing current to flow in both biasing directions equally well. The qualities of both types of connections play an essential role in the performance of integrated circuit devices. Here we discuss the Schottky junction.

Schottky junctions are one of the most used diodes in photodetectors applications. A Schottky junction is formed between a semiconductor and a semi-transparent metal contact. By Mott-Schottky theory, there is an electrostatic barrier between the semiconductor and metal due to the difference in work functions ($q"\emptyset"\_B$) of semiconductor and metal. This gives rise to the rectifying property in Schottky junctions. The formation of the Schottky junction is characterised by band bending at the interface due to potential barriers. It is given by the difference between the work function of metal and semiconductors [29].

Further, the band bending and electrostatic barrier leads to the formation of Schottky barrier height, which is of utmost importance in Schottky junctions. The Schottky barrier height is a function of the metal and semiconductor, and hence different metal contacts will form different Schottky barrier heights with the same semiconductor. In n-type semiconductor/Schottky junction, the barrier height is against the flow of electrons between Schottky junction, while in p-type semiconductor/Schottky junction, the barrier height is against the flow of holes.

Figure 1.9 shows the band diagram between the n-type semiconductor-based Schottky junction. The Schottky junctions are characterised by majority charge carrier transport as there is no diffusion of charge carriers. In contrast, the distribution of charge carriers across the junction is observed in a p-n junction. Hence, the charge transport properties in a Schottky junction depend on the semiconductors' heterojunction interface and surface states. For the smooth transition of charge carriers, the interface of the Schottky junction should be free of surface defects and impurities. Further, Schottky junctions possess high quantum efficiency, high responsivity and low turn-on voltage [29].
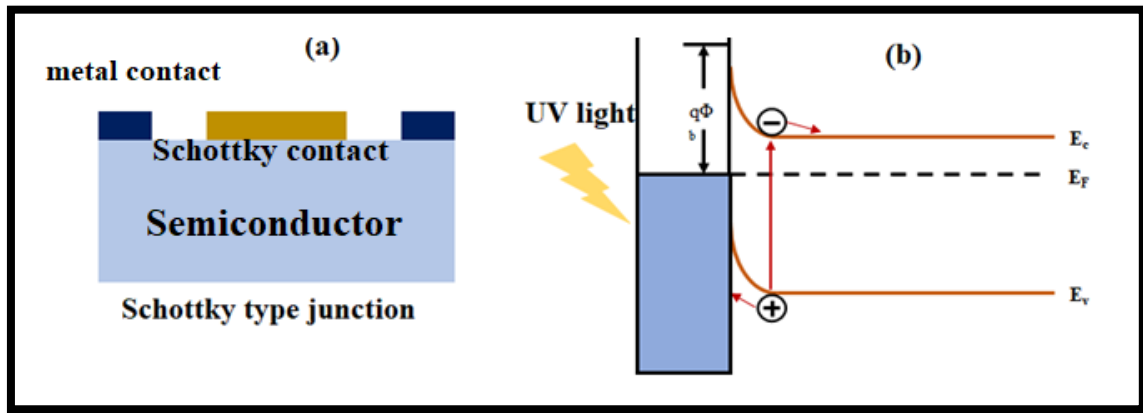
Figure 1.9: (a) The formation of a typical Schottky junction (b) shows the band diagram of a typical Schottky junction with band bending and Schottky barrier height.

However, it does have some disadvantages of metal contact thickness, loss of UV radiation to thick metal contacts, surface state affecting the charge carrier transport. [29]. Nevertheless, the Schottky junction is widely used for UV photodetectors with conventional metal electrodes. I have studied the GaN and Ga_2O_3 based Schottky junctions with hBN and their UV photoresponsivity in this study.

1.2.2   p-n junction devices

A p-n junction is formed by integrating a p-type semiconductor and an n-type semiconductor to create either a p-n homojunction or a p-n heterojunction. In the p-n junction, the depletion region is instantaneously formed with charge diffusion.   In the p-n heterojunction, the n-type semiconductor has an excess of electrons concerning p-type semiconductor. The p-type of semiconductors have a lot of holes concerning n-type semiconductors, and thus when a p-n junction is formed, electrons from n-type diffuse into p-type and vice versa [29]. This leads to the formation of a depletion region, defined as the region at the interface of the junction where generated majority charge carriers are diffused away.

Further, when UV irradiation with energy equal to or greater than the material's bandgap is incident, it creates additional electron-hole pairs on both sides of the junction. After the equilibrium is attained at the depletion region, the electron-hole pair stops to diffuse into the depletion region and starts to get separated and generate a photocurrent detected at the external circuit. The band diagram and device structure of a typical p-n junction is given in **Figure 1.10.**
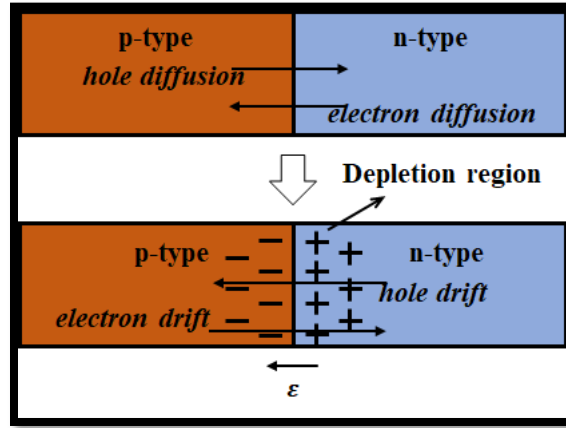
Figure 1.10: The formation of a depletion layer at the interface of the typical p-n junction.

The charge transport phenomenon in a p-n junction is due to minority charge carriers as the majority charge carriers are diffused in the depletion region. This results in less effect of interface quality on the charge transport across the interface junction [30]. This separates the p-n junction from the Schottky junction. Further, p-n junctions have higher turn-on voltage than Schottky junctions. Schottky barrier photodiodes have been studied extensively and found application as UV detectors. The following table presents some advantages of Schottky junction devices over p-n junction photodiodes: fabrication simplicity, absence of high-temperature diffusion processes, and high speed of response.

Table 1 shows the comparison of properties between Schottky and p-n junction [29-30].

	Property	Schottky junction	p-n junction
1)	Charge carrier	**Majority charge transport due to the absence of diffusion**	**Minority charge transport due to diffusion.**
2)	Effect of surface states	**Surface state effect on charge carrier transport**	**Not applicable**
3)	Turn on voltage	**Low turn-on voltage**	**High turn-on voltage**
4)	Switching speed	**High switching speed**	**Low switching speed**
5)	Loss of radiation	**Loss of incident radiation due to metal contact thickness**	**No such issue in p-n junction**

Thus, as discussed above, both Schottky and p-n junctions have advantages and disadvantages. However, they are the most studied device structures for UV photodetector application. They possess collective advantages over other types of junctions such as MSM (metal-semiconductor-metal) based p-n junction regarding ease of fabrication and easy operation, high responsivity, less loss of UV irradiation to metal contacts etc. Hence, I have worked on both Schottky junction and p-n junctions based on GaN and Ga2O3 semiconductors for the present research thesis. The organization of the thesis

1.3 Organization of the thesis

The Chapters contents of the thesis are briefly described as follows;

Chapter 1 Includes a brief description of the research background, the purpose of the study, and the organisation of the thesis.

Chapter 2 Self-assembled C_{60} fullerene cylindrical nanotubes by the LLIP method. Explained properties of the material and its uniqueness in organic electronics. Discussed on Scope to use in the many opt-electronic applications such as FET and Solar Cells.

Chapter 3 Temperature-dependent device properties of γ-CuI and β-Ga_2O_3 heterojunctions It was relieving the interface properties of p-type γ-copper iodide (γ-CuI) and n-type β-gallium oxide (β-Ga_2O_3) heterojunction. Discussed stability at a temperature as high as 473K. Confirmed the current transport mechanism at the heterojunction interface by analysing the temperature-dependent current-voltage characterization.

Chapter 4 Characteristics of vertical Ga_2O_3 Schottky junctions with the interfacial hexagonal boron nitride film. Fabrication of a Ni/β-Ga_2O_3 Schottky junction device with an hBN interface layer. The hBN film was synthesized and transferred by the wet chemical transfer method.

Chapter 5 Summary and Conclusion of the research work in detail.

1.4 References:

1. Kroto, H., Heath, J., O'Brien, S. et al. C_{60}: Buckminsterfullerene. Nature 318, 162–163 (1985).

2. Paul H.Ẅobkenberg, Donal D.C. Bradley, David Kronholm, Jan C. Hummelen, Dago M. de Leeuwd, Michael Colle, Thomas D. Anthopoulos Synthetic Metals 158 (2008) 468–472.

3. Joshua N. Haddock, Xiaohong Zhang, Benoit Domercq, Bernard Kippelen. Organic Electronics 6 (2005) 182–187.

4. S. P. Tiwari, E. B. Namdas, V. Ramgopal Rao, Senior Member, IEEE, D. Fichou, and S. G. Mhaisalkar, IEEE Electron Device Letters, Vol. 28, No. 10, Oct 2007.

5. Tommie W. Kelleya1, Dawn V. Muyresa, Paul F.Baudea1, Terry P. Smitha and Todd D. Jonesa, 2003 MRS Spring Meeting. MRS Proceedings / Volume 771, 2003.

6. T. Kanbara, K. Shibata, S. Fujiki, Y. Kubozono, S.Kashino, T. Urisu, M. Sakai, A. Fujiwara, R. umashiro, K. Tanigaki; N-channel field-effect transistors with fullerene thin films and their application to a logic ate circuit; Chemical Physics Letters, Volume 379, Issues 3–4, 26 September 2003, Pages 223–229.

7. Th. B. Singh, N. Marjanović, G. J. Matt, and N. S.Sariciftci; Nonvolatile organic field-effect transistor memory element with a polymeric gate electret; Appl. Phys. Lett., Vol. 85, No. 22, 29 November 2004.

8. Shinuk Cho, Jung Hwa Seo, Kwanghee Lee, and Alan J.Heeger; Enhanced Performance of Fullerene n-Channel Field-Effect Transistors with Titanium Sub-Oxide Injection Layer; Adv. Funct. Mater. 2009, 19, 1459– 1464.

9. Kubota, Y.; Watanabe, K.; Tsuda, O.; Taniguchi, T. Science 2007, 317 (5840), 932−934.

10. Kho, J. G.; Moon, K. T.; Kim, J. H.; Kim, D. P. J. Am. Ceram. Soc. 2000, 83 (11), 2681−2683.

11. L. Dong et al., Sci Rep., vol. 7, p. 40160, 2017.

12. Pease, R. S. Nature 1950, 165 (4201), 722−723.

13. Kho, J. G.; Moon, K. T.; Kim, J. H.; Kim, D. P. J. Am. Ceram. Soc. 2000, 83 (11), 2681−2683.

14. Sugino, T.; Tai, T. Jpn. J. Appl. Phys., Part 2 2000, 39 (11A), L1101−L1104.

15. Song, L.; Ci, L.; Lu, H.; Sorokin, P. B.; Jin, C.; Ni, J.; Kvashnin, A. G.; Kvashnin, D. G.; Lou, J.; Yakobson, B. I.; Ajayan, P. M. Nano Lett. 2010, 10 (8), 3209−15.

16. Chen, Y.; Zou, J.; Campbell, S. J.; Le Caer, G. Appl. Phys. Lett. 2004, 84 (13), 2430−2432.

17. Watanabe, K.; Taniguchi, T.; Kanda, H. Nat. Mater. 2004, 3 (6), 404−409.

18. Dean, C. R.; Young, A. F.; Meric, I.; Lee, C.; Wang, L.; Sorgenfrei, S.; Watanabe, K.; Taniguchi, T.; Kim, P.; Shepard, K. L.; Hone, J. Nat. Nanotechnol. 2010, 5 (10), 722−726.

19. Naumov, I.; Bratkovsky, A. M.; Ranjan, V. Phys. Rev. Lett. 2009, 102 (21), 217601

20. X. Lu, M. Yu, H. Huang, and R. S. Ruoff, Nanotechnology **10**, 269 (1999).

21. Sumiyoshi, H. Hyodo, and K. Kimura, J. Solid State Chem. **187**, 208 (2012).

22. Y. Kubota, K. Watanabe, O. Tsuda, and T. Taniguchi, Science **317**, 932 (2007).

23. C. R. Dean, A. F. Young, I. Meric, C. Lee, L. Wang, S. Sorgenfrei, K. Watanabe, T.Taniguchi, P. Kim, K. L. Shepard, and J. Hone, Nat. Nanotechnol. 5, 722 (2010).

24. L. Britnell, R. V. Gorbachev, R. Jalil, B. D. Belle, F. Schedin, A. Mishchenko, T.Georgiou, M. I. Katsnelson, L. Eaves, S. V. Morozov, N. M. R. Peres, J. Leist, A. K.Geim, K. S. Novoselov, and L. A. Ponomarenko, Science 335, 947 (2012).

25. Q. Peng, Z. Wang, B. Sa, B. Wu, and Z. Sun, Sci. Rep. **6**, 31994 (2016).

26. G. R. Bhimanapati, N. R. Glavin, and J. A. Robinson, in Semicond. Semimet., edited by J.J. B. and C. J. Francesca Iacopi (Elsevier, 2016), pp. 101–147.

27. N. Kostoglou, K. Polychronopoulou, and C. Rebholz, Vacuum **112**, 42 (2015).

28. Britannica, The Editors of Encyclopaedia. "Walter Schottky". Encyclopedia Britannica, 19 Jul. 2021,

29. Y. Zou et al., Sensors, vol. 18, p. 2072, 2018.

30. B. D. Boruah, Nanoscale Adv., vol. 1, pp. 2059-2085, 2019.

31. Yao, K., Chen, P., Zhang, Z. et al. Synthesis of ultrathin two-dimensional nanosheets and van der Waals heterostructures from non-layered γ-CuI. npj 2D Mater Appl 2, 16 (2018).

32. Takayoshi Oshima, Takeya Okuno, Naoki Arai, Norihito Suzuki, Shigeo Ohira and Shizuo Fujita, 2008 Appl. Phys. Express 1 011202.

33. N. Prakash, M. Singh, G. Kumar, A. Barvat, K. Anand, P. Pal, S. P. Singh and S. P. Khanna, Appl. Phys. Lett. 2016, 109, 242102.

34. G. Kalita, M. D. Shaarin, B. Paudel, R. Mahyavanshi, M. Tanemura, Appl. Phys. Lett. 2017, 111, 013504.

35. High-temperature Ultraviolet Photodetectors: A Review, Ruth A. Miller, Hongyun So, Thomas A. Heuser, and Debbie G. Senesky

36. Dong, L., Jia, R., Xin, B. et al. Effects of oxygen vacancies on the structural and optical properties of β-Ga2O3. Sci Rep 7, 40160 (2017).

CHAPTER 2

Self-assembled C$_{60}$ fullerene cylindrical nanotubes by the LLIP method.

2.1 Introduction

For the past few years, organic electronic devices have been emerging into the market. But to pave the way for further products, improvements in device performance have to be accomplished. Besides new materials, this requires a deeper understanding of the interplay between the active materials. Of particular significance in all electronic devices are interfaces between different layers, and controlling the morphological and electronic structure of molecules at interfaces is the key challenge. A lot of work has been done to understand the correlation between chemical structure, thin-film morphology, and electrical properties of organic molecules at interfaces. [21-24] However, the ultimate goal is to design materials that form defined ordered structures via self-organization and thus ease the process to obtain desired properties. In this study, a novel approach has been discovered to improve the chances of self-assembly materials in the field of organic electronic devices such as thin-film transistors (TFTs). Hence, I would like to introduce the Self-assembly C60 fullerene materials synthesized by (LLIP) and got the FNCT Fullerene Nano Cylindrical Tubes as a unique material that can be used for charge transport material in organic thin-film transistors. As promising devices in future flexible electronics, the material properties are well stable and unique in atmospheric conditions. We have observed this material for six months but no change in properties with a long-lasting result. So it's considered as a novel material that has scope to use in the many opt-electronic applications such as FET and Solar Cells. [25]

Due to this large variety in scope for design, Self-assembly materials have been successfully integrated into various organic electronic devices, such as organic thin-film transistors (TFTs),

[26-27] organic photovoltaics (OPV) [28], and organic memory devices. [29-30] Even semiconducting properties can be included in the molecules, which leads to organic semiconducting monolayers. These films can be incorporated as active layers in a thin film.

C_{60} Fullerene Nano Cylindrical Tubes (FNCT) were synthesized by an (LLIP) method using m-Xylene as a saturating solvent and TBA (Tert-butyl alcoholic) as a precipitation agent leading to the formation of FNCTs with uniquely structured and well-oriented size and shape. The experiment was conducted in a closed atmosphere maintaining a low temperature. The main advantage of these structures is that they are stable for up to 5 months at normal room temperature. The characterisation was done to the FNCTs and concluded that semiconducting properties had been observed in the nanostructures that can be used to apply solar cells, FET transistors, Etc. Fullerene C_{60} is one of the best-investigated materials from the nanomaterial field from the family of carbons due to its utilization in potential applications such as semiconductors and optoelectronic devices. [1-3] Nanotechnology is an emerging field of growing importance. The driving force behind the search for Nano-sized materials is the continuing demand for minimization in electronic devices' dimensions while optimizing their performance. With the reduction in size and shape, these materials exhibit unique optoelectronic properties, which are size-dependent in contrast to their corresponding bulk materials. The investigation of self-assembled fullerene nanostructures paved a new era for nanotechnology research. In current scientific technology, scientists are focusing on recognizing the properties of the atoms and molecules, which enable them to arrange themselves in different shapes and patterns, which can be possible by self-assembly [4-5]. Due to the increasing technological advancements in the field of nanotechnology, self-assembly presents the scope of providing an alternative to a bottom-up approach in which the precursor materials get assembled to form potential device components and utilize them in Nanoelectronics photovoltaics, biological applications, Etc. [6-8] The as-prepared self-assembled semiconducting FNCT

exhibited excellent electron transport properties benefiting from their molecular ordering and the lack of grain boundaries, which attract significant attention to the preparation, characterization, and further fabrication of electronic devices [9]. These investigations not only give a direct correlation between the molecular architecture and the molecular packing in their solid states but also shed light on the charge transporting between molecules, which can hopefully provide a guideline for the development of semiconducting materials from the perspective of molecular architecture and molecular interactions [10]. Future applications of nanostructured-assembled materials might be numerous, including new electronic devices, in which organic molecular wires could be connected to form nanoelectronics circuits or atomic switches [11-15], nanoparticles, quantum dots, which could be used in quantum electronics for storing individual bits of information, single-molecule sensing through integrated supramolecular recognition, targeted drug-delivery vehicles, etc. The production of shape- and size-controlled fullerene crystals would enhance the utility of these molecules in tailoring their properties. Notably, we will mainly describe the formation of nanostructures from unmodified fullerene units [16-18]. However, preparing FNCT with the desired size, shape, and structure is still a significant challenge in productivity and repeatability.

2.2 Synthesis of C_{60} Fullerene

Pristine fullerene (C_{60}) powder with a purity greater than 99% was bought from Sigma Aldrich. m-xylene (C_8H_{10}) and tert-butyl alcohol (TBA) $(CH_3)_3COH$ The preparation of C_{60} saturated solution was accomplished by dissolving pristine C_{60} in m-xylene. The dissolving process is carried out in an ultra-sonicate. Firstly, 3mg was dissolved in 3 ml m-xylene for better mixture use ultra-sonicate for 10 min. The change in color of the solution from transparent to purple indicates
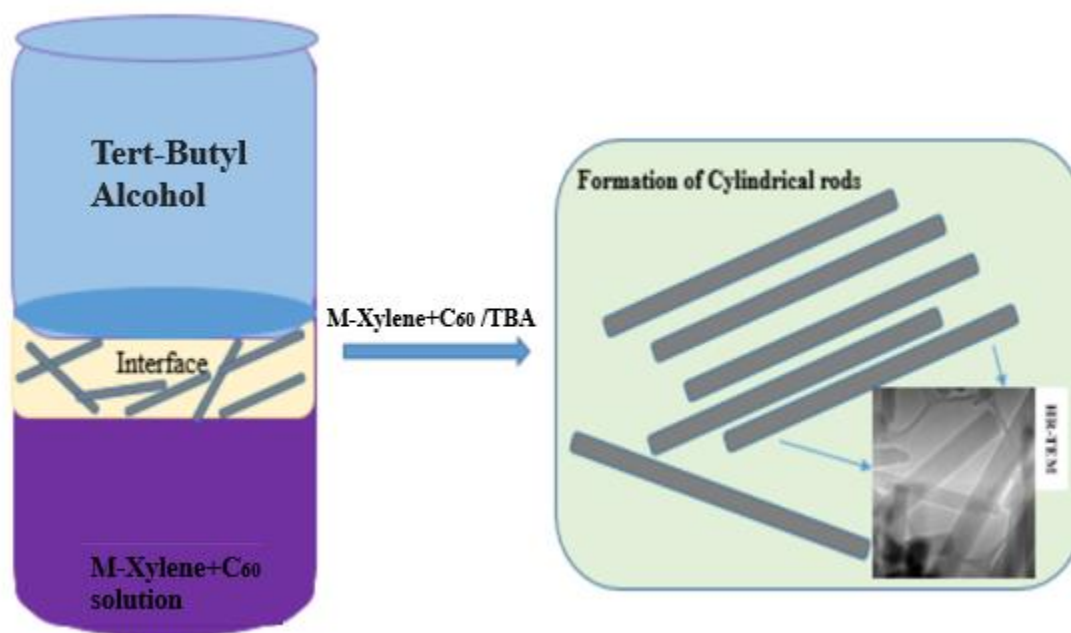
Figure 2.1 Schematic diagram of self-assembled C_{60} fullerene.

that C_{60} has been dissolved in a solvent with some un-dissolved fullerene. After sonication, filter the excess C_{60}, which gets precipitated at the bottom. The liquid-liquid interfacial precipitation method was employed to prepare cylindrical tubes. A TBA of 6 ml was added to the C_{60} saturated solution dropwise. The complete process is carried out at a low temperature (0° -5 °C), which was achieved by using an ice bath. In this experiment, several stages in forming hexagonal crystals were observed. Furthermore, they are graphically explained in the schematic representation above.

2.3 Results and Discussion

Fullerene cylindrical nanotubes morphology has been observed by HR-SEM analysis confirmed that the shape of the obtained self-assembled cylindrical tubes is porous in structure with an actual diameter of the cylindrical Nanotubes. The material has formed by the mixture of the M-xylene and TBA. The cylindrical tube is shown in the above (a) shows the porous structure nanotubes in the scale of 1μm and (b) shows the bunch of nanotubes within 2μm scale.
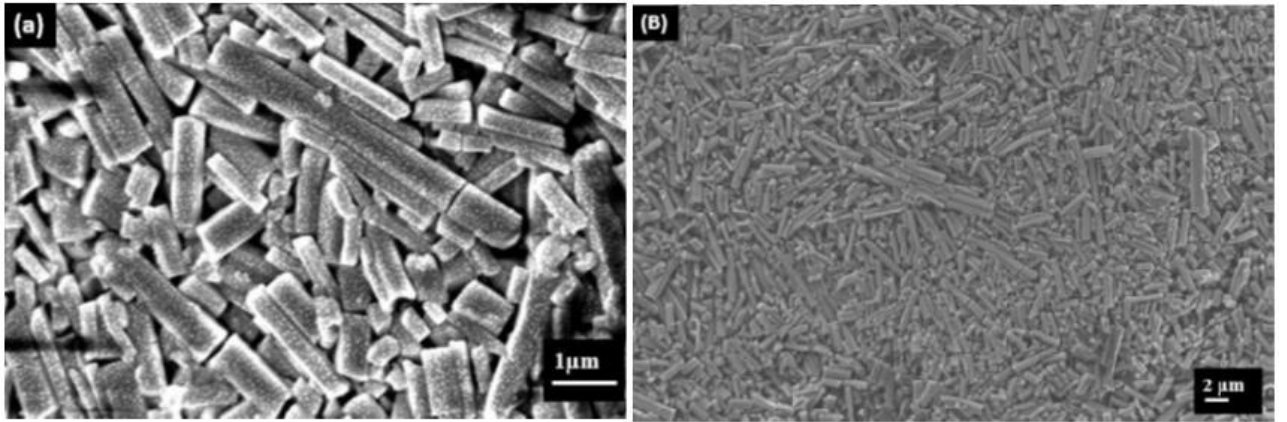
Figure 2.2 SEM images of C_{60} FNCT with even diameters; (a)&(b) ϕ 6.6mm.
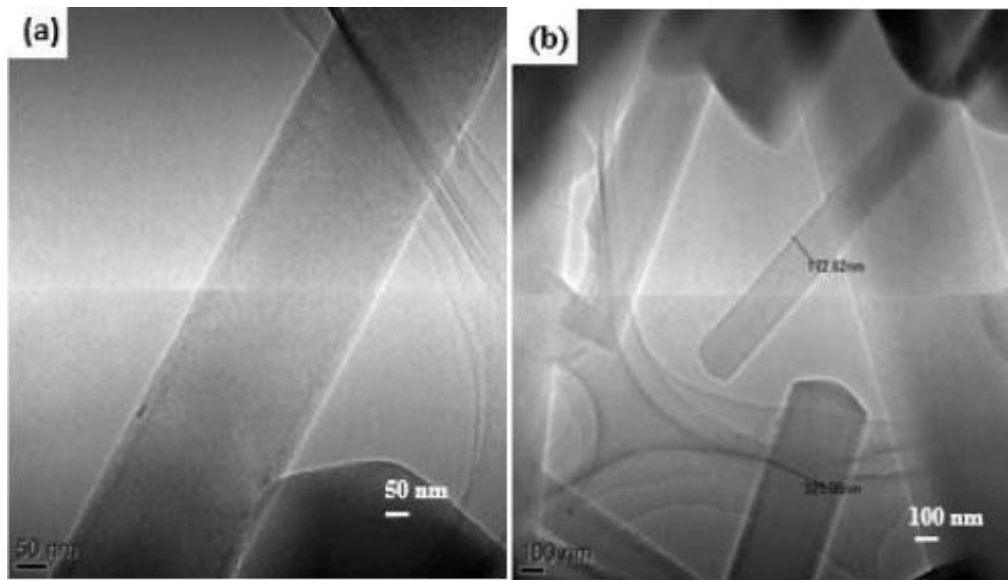
Figure 2.3 HR TEM observations (a) under 50nm scale (b) FNCT under 100nm scale.

The Transmission electronic microscope was performed by JEOL JEM-2100F high-resolution TEM operated at 200kv. The self-assembled sample was doped on a copper grid and dried to analyze the self-assembled fullerene cylindrical Nanotubes assembled by two interfaces with a long cylindrical tube structure. Which has been observed by the TEM **figure 2.3** (a) shows the cylindrical shape tube with a smooth surface (b) different size cylindrical with different size as 325.06nm and one more rod with little thin in shape with 112.62nm can be observed by the TEM.

XRD pattern of the self-assembled fullerene Nanotubes crystallite size is 33nm with the parameter, the average crystal size was calculated as a=B=C= 14.26nm. The alpha, beta, and gamma are equal to 90º with considered a cubic structure. Here we can observe the four major peaks in the graph as 10.9663, 18.3489, 20.5587, and 21.0048, where the (h, k,l) values are considered for the respective above mentioned peaks (111), (220), (311), and (222) confirmed by JCPDF file No 82-0505.
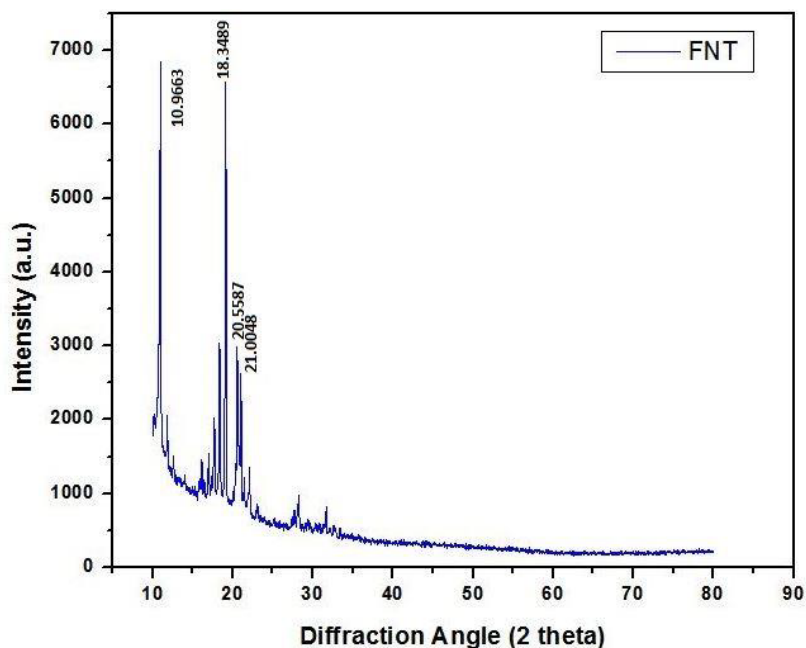
Figure 2.4. XRD patterns of the ultra-rapidly formed fullerene nanotube.

FT-IR spectroscopy was performed on the sample synthesized with an m-xylene/TBA with 1:2 ratios. To analyze the functional group of the cylindrical nanotubes, the prominent most significant peak was observed in **figure 2.5** are at 527, 576, 1429 cm[1]. Two additional peaks were formed at 3446.27cm^{-1}. where most of the peaks are similar for carbon materials. [12]
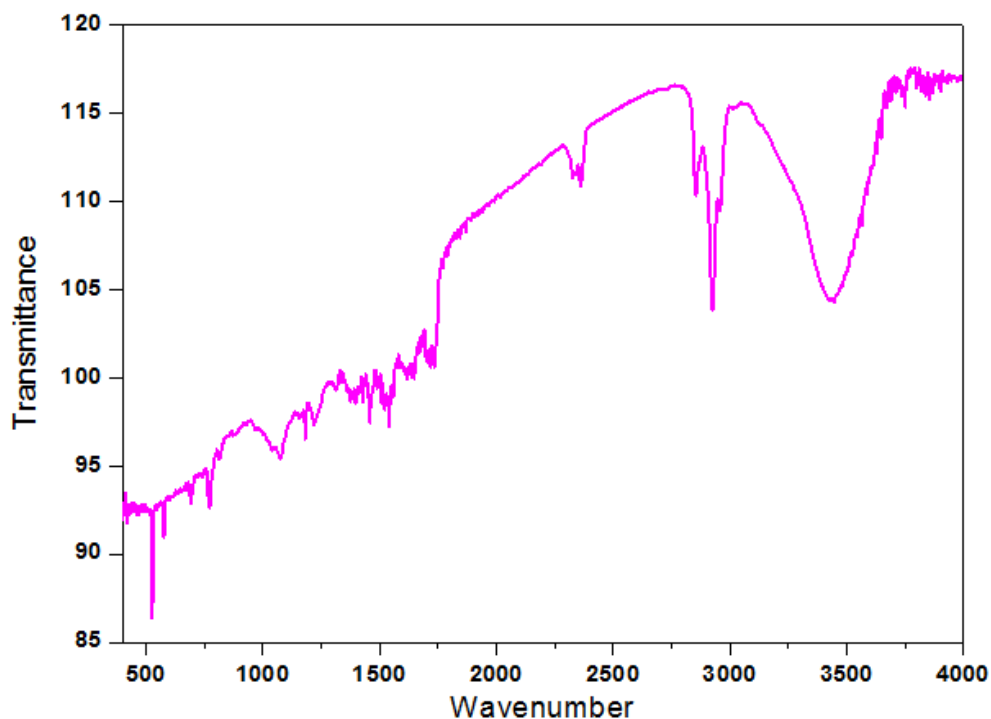
Figure 2.5. FTIR spectrum of cylindrical nanotubes

UV-Visible Spectroscopy has been used to observe the suspension of the fullerene cylindrical nanotube was diluted in the methanol solvent and scanned in the range of 200- 700 nm, and the result was shown in the Figure6. As we can observe from figure 2.6, the self-assembled solution had an absorption in the range of 200 -400 nm with a peak wavelength of 250nm,
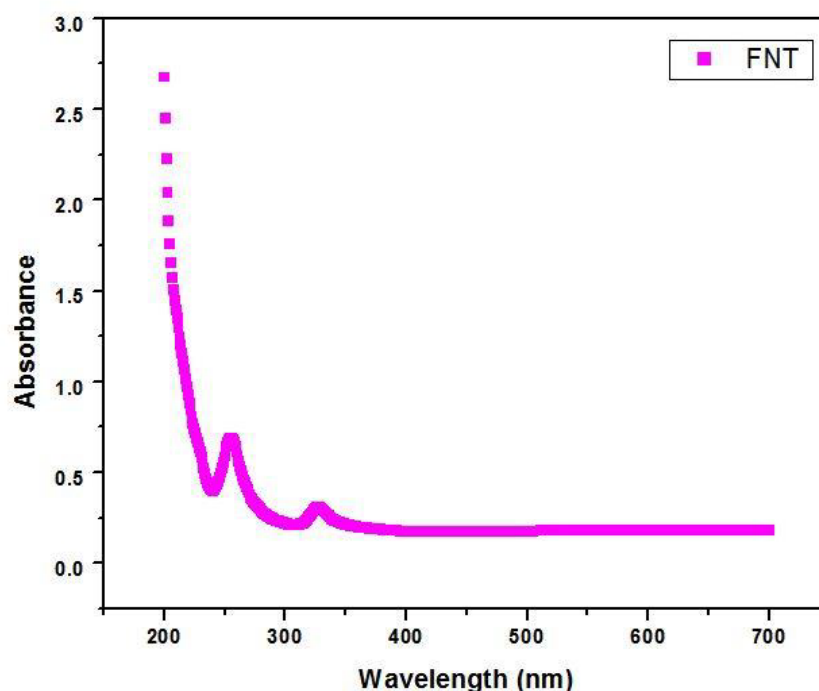
Figure 2.6. UV-vis spectroscopy of the cylindrical tubes aggregated suspension(diluted)

Raman spectroscopy was performed by JASCO NRS- 5100 Nps laser Raman. It is used to analyze the self-assembled cylindrical tubes. Here we can observe the two strong peaks in **figure 2.7.** The band ranges from 1400-1500 cm-1, and another strong peak at 1500 -1600 cm $^{-1}$. Both peaks correspond to have D and G bands. The sample preparation for the analysis of the Raman spectroscopy sample has dried on the silicon wafer. The self-assembled Raman spectroscopy analysis results were similarly performed by fullerene C_{60} [19].
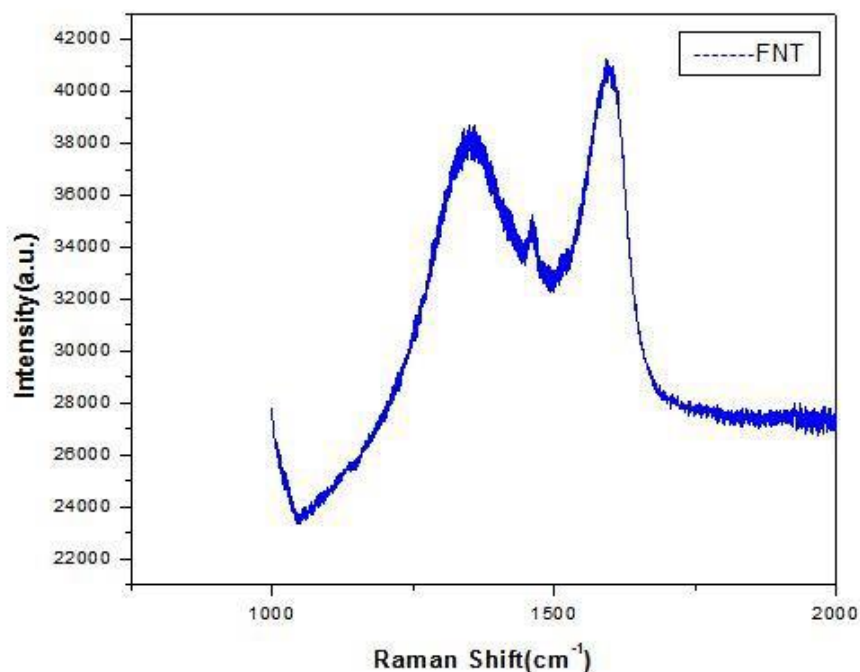
Figure 2.7. Raman scattering analysis for self-assembled cylindrical nanotubes.

2.4 Conclusion:

The synthesis of the self-assembled fullerene Nanotube is evenly distributed with the porous structure for the cylindrical tubes, and the structure shows the opt electronic properties. By confirming the crystal size at 32 nm with XRD and the cylindrical nanotubes, the shape was confirmed by the FESEM and TEM, which this material can be used in the FET transistors for electron transport materials. In our further work, we would like to use this material for the FET transistor. The properties of the material are well stable and unique in atmospheric conditions. We have observed this material for 6 months but no change in properties with a stable result. So it's considered as a novel material that has scope to use in the many opt-electronic applications such as FET and Solar Cells.

2.5 References:

[1] S.Banya, T. Akiyama, D. Izumoto, A. Suzuki, T. Oku,"Formation of Thin Films of Densely Packed Fullerene Diaminoethane Adduct Micro particles at aLiquid/Liquid Interface and Their Photo electrochemical Applications" in Chem. Lett. Japan, 2015, 44, pp. 489–491.

[2] L. K. Shrestha, J. P. Hill, T.Tsuruoka, K. Miyazawa,K.Ariga, "Surfactant-Assisted Assembly of Fullerene(C_{60}) Nanorods and Nanotubes Formed at a Liquid−Liquid Interface" in Langmuir 2013, 29, pp. 7195−7202.

[3] H. Liu, X. Cao, Y. Wu, Q. Liao, A. J. Jimenez, F.Wurthner, H. Fu, "Self-assembly of octachloroperylene diimide into1D rods and 2D plates by manipulating the growth kinetics for waveguide applications" Chem. Commun., 2014, 50, pp.4620 – 4623.

[4] N. Chandrasekhar, S. Basak, M. A. Mohiddon, R.Chandrasekar, "Planar Active Organic Waveguide and Wavelength Filter: Self-Assembled meso- Tetratolylporphyrin Hexagonal Nanosheet" ACS Appl. Mater. Interfaces 2014, 6, pp. 1488−1494.

[5] L. Shrestha, Q.Ji, T. Mori, K.Miyazawa, Y. Yamauchi, J. P. Hill, K. Ariga, "Fullerene Nanoarchitectonics: FromZero to Higher Dimensions" Chem. Asian J. 2013, 8, pp.1662 – 1679.

[6] N. Chandrasekhar, R.Chandrasekar, "Reversibly Shape- Shifting Organic Optical Waveguides: Formation of Organic Nanorings, Nanotubes, and Nanosheets" Angew. Chem. Int. Ed. 2012, 51, pp. 3556 –3561.

[7] C. Park, H.J. Song, H. C. Choi, "The critical effect of solvent geometry on the determination of fullerene (C_{60}) 0self-assembly into dot, wire and disk structures" Chem. Commun., 2009, pp. 4803–4805.

[8] M. S. Amera, T. K. Todd, J. D. Busbee, "Effect of linear alcohol molecular size on the self-assembly of fullerene whiskers" Materials Chemistry and Physics 130, 2011, pp. 90– 94.

[9] L.Zheng,Y. Han, "Solvated Crystals Based on [6,6]- Phenyl-C61-butyric Acid Methyl Ester(PCBM) with the

Hexagonal Structure and Their PhaseTransformation" J. Phys. Chem. B 2012, 116, pp. 1598−1604.

[10] B.Wang, X.Gao, G.Piao, "Fabrication of C_{60} Fullerene Nanofibers by Volatile Diffusion Method" Hindawi Publishing Corporation Journal of Nanomaterials, 2013, Article ID 646040, pp. 5.

[11] J N. Tisserant, P A. Reissner,S. Jenatsch,H.Beyer,R.Hany, A.Stemmer "Interfacial selfassembly of nanoporous C_{60} thin films" RSC Adv., 2016, 6, 23141–23147.

[12] K.T. Wong, D.M Bassani"Energy transfer in supramolecular materials for new applications in photonics and electronics" NPG Asia Materials (2014) 6.

[13].A.NigamG.Schwabegger,M.Ullah,R.Ahmed,I.I.Fishchuk,A.kadashchuk,C.simbrunner,H.Sitter,M.Premaratne,V.R.Rao"Strain induced anisotropic effect on electron mobility in C_{60} based organic field effect transistors "Applied physics letters, 2012, 101, 083305.

[14] J.Geng, W. Zhou, P.Skelton, W.Yue, I.A. Kinloch, A.H. Windle, B.F.G. Johnson"Crystal Structure and Growth Mechanism of Unusually Long Fullerene (C_{60}) Nanowires" J. AM. CHEM. SOC. 2008, 130, 2527-2534.

[15] S.H.Choi,C.C.Liman, S.Kramer,M.L.Chabinyc,E.J. Kramer"Crystalline Polymorphs of [6,6]-Phenyl-C61- butyric Acid n-Butyl Ester (PCBNB)"J. Phys. Chem. B 2012, 116, 13568−13574.

[16]   H.R.Barzegar,F.Nitze,A.Malolepszy,L.Stobinski,C.W.T   ai,T.Wagberg,"Water Assisted Growth of C_{60} Rods and Tubes by Liquid–Liquid Interfacial Precipitation Method" Molecules 2012, 17, 6840-6853.

[17] M.Sathish,K.Miyazawa"Size-Tunable Hexagonal Fullerene (C_{60}) Nanosheets at the Liquid-Liquid Interface"J. AM. CHEM. SOC. 2007, 129, 13816-13817.

[18]   H.X.Ji,J.S.Hu,Q.X.Tang,W.G.Song,C.R.Wang,W.P.Hu,   L.j.Wan,S.T.Lee"Controllable Preparation of Submicrometer Single-Crystal C_{60} Rods and Tubes Trough Concentration Depletion at the Surfaces of Seeds"J. Phys. Chem. C, Vol. 111, No. 28, 2007 10499.

[19] R.Saran, V.Stolojan,R.J. Curry"Ultrahigh Performance C_{60} Nanorod Large Area Flexible Photoconductor Devices via Ultralow Organic and Inorganic Photodoping"Scientific Reports,2014,4,5041

[20] R.G.Shrestha,L.K.Shrestha,A.H.Khan,G.S.Kumar,S.Ac harya,K.Ariga, "Demonstration of Ultrarapid Interfacial Formation of 1D Fullerene Nanorods with Photovoltaic Properties"ACS Appl. Mater. Interfaces 2014, 6, n15597−15603.

[21] J. Veres, S. Ogier, G. Lloyd and D. De Leeuw, Chem. Mater., 2004, 16, 4543–4555.

[22] N. Koch, ChemPhysChem, 2007, 8, 1438–1455.

[23] H. Dong, L. Jiang and W. Hu, Phys. Chem. Chem. Phys., 2012, 14, 14165–14180.

[24] T.Schmaltz,   A. Khassanov,   H.Steinrück,   A.Mager, A.Hirschc, M.Halik, Tuning the molecular order of C_{60}-based self-assembled monolayers in field-effect transistors, Nanoscale, 2014,6, 13022-13027

[25] PS. Karthik, Y.Shimo, Z. Lin, R.V. K. Rao, X. Gong1, M.Yoshida, M.Hada, T. Nishikawa, Y. Hayashi, Carbon nanostructures synthesized via self-assembly (LLIP) and its application in FET. IEEE 17-20 April 2016

26. M. Halik, H. Klauk, U. Zschieschang, G. Schmid, C. Dehm, M. Schutz, S. Maisch, F. Effenberger, M. Brunnbauer and F. Stellacci, Nature, 2004, 431, 963–966.

 27. T. Sekitani, U. Zschieschang, H. Klauk and T. Someya, Nat. Mater., 2010, 9, 1015–1022.

28. T. Stubhan, M. Salinas, A. Ebel, F. C. Krebs, A. Hirsch, M. Halik and C. J. Brabec, Adv. Energy Mater., 2012, 2, 532–535

29. M. Burkhardt, A. Jedaa, M. Novak, A. Ebel, K. Voïtchovsky, F. Stellacci, A. Hirsch and M. Halik, Adv. Mater., 2010, 22, 2525–2528

30. T. Sekitani, T. Yokota, U. Zschieschang, H. Klauk, S. Bauer, K. Takeuchi, M. Takamiya, T. Sakurai and T. Someya, Science, 2009, 326, 1516–1519.

Chapter 3

Temperature-dependent device properties of γ-CuI and β-Ga₂O₃ heterojunctions

3.1 Introduction

Among ultra-wide bandgap semiconductors, gallium oxide (Ga_2O_3), with a bandgap of 4.5–4.9 eV, has attracted significant attention for deep ultraviolet (DUV) photonics and power electronic device applications [1, 2]. β-Ga_2O_3, with a monoclinic structure and lattice parameters of a = 12.22 Å, b = 3.0 Å, and c = 5.8 Å, is the most stable form among all the polymorphs of Ga_2O_3 at room temperature [3, 4]. It has been reported that electron mobility as high as 300 cm^2 $V{-1}$ $s{-1}$ can be achieved in β- Ga_2O_3 at room temperature. β- Ga_2O_3 possesses a critical field strength higher than that of Si, SiC, and GaN semiconducting materials. The predicted critical field (E_{br}) for β- Ga_2O_3 is 8 mv cm−1, whereas the measured E_{br}, is 3.8 MV cm^{-1} [5]. Owing to its high chemical and mechanical stabilities (Young's modulus of β- Ga_2O_3 = 232 GPa) and thermal stability (melting point 1820 °C), it is well suited for applications such as solar-blind photodetectors [6], light-emitting devices, and power electronic devices [7, 8]. β- Ga_2O_3 exhibits n-type semiconducting behavior due to the presence of oxygen vacancies, similar to many other oxide semiconductors [9]. Most device fabrication approaches have adopted the Schottky junction or p-n heterojunction structure for practical applications [10, 11]. Thus, suitable materials for fabricating a Schottky or p-n junction of Ga_2O_3 are critical in achieving high device performance. β- Ga_2O_3-based Schottky barrier diodes (SBDs) have been investigated for the development of high-voltage devices as well as solar-blind photodetectors [10, 12, 13]. Metal electrodes, such as Au (gold), Pt (platinum), and Ni (nickel), have been explored for the fabrication of β- Ga_2O_3- based SBDs [3, 4, 14, 15]. We

have demonstrated the integration of graphene with β- Ga_2O_3 for the fabrication of deep-UV photo responsive SBD devices. SBDs are majority carrier devices, where the interface between the Ga_2O_3 and metal contacts plays a significant role in the device properties [14, 15]. By contrast, p-n junctions are minority carrier devices, which are important in achieving a low reverse saturation current and high breakdown voltage. Thus, a suitable p-type wide-bandgap semiconductor as a counterpart for the n-type Ga_2O_3 is significant for device fabrication [15, 16]. γ-CuI with a bandgap of ~ 3.1 eV and p-type carrier mobility of ~ 40 cm^2 $V{-1}$ $s{-1}$ has been investigated for heterojunction devices with β- Ga_2O_3 [17, 18]. The lattice mismatch between the cubic phase γ-CuI (111) and β- Ga_2O_3 along the c-axis is approximately 2%, indicating the possibility of fabricating a compatible heterostructure of γ-CuI (111) and β- Ga_2O_3 for heterojunction device applications [19–22]. Previously, Ranade et al. reported the integration of γ-CuI with gallium nitride (GaN), which is a III nitride wide bandgap semiconductor, to form a p-n heterojunction with high-temperature stable photovoltaic action [18]. The successful fabrication of a γ-CuI/GaN heterojunction motivated us to explore the integration of p-type γ-CuI with β- Ga_2O_3. In our previous study, we reported the observation of a DUV radiation-induced photovoltaic action for the γ-CuI/β- Ga_2O_3 heterojunction. In contrast to our previous studies, herein, we revealed the behavior of the heterojunction interface in the γ-CuI/β- Ga_2O_3 material

system, which is significant for understanding its defect states, current transport mechanism, and temperature stability [23]. The temperature-dependent device characteristics were studied in the temperature range 273–473 K to investigate the heterojunction interface. With an increase in temperature, a gradual decrease in the ideality factor and an increase in barrier height were observed, indicating a barrier inhomogeneity at the heterojunction interface. Interestingly, we can correlate the electrical hysteresis and barrier inhomogeneity behavior of the γ-CuI/β- Ga_2O_3 heterojunction device, thereby revealing the influence of the interface states on these parameters.

3.2 Materials and Methods

Here, we used Sn-doped, n-type single-crystal β- Ga_2O_3 (thickness of 650μm, donor concentration of 3×10^{18} cm^{-3}) purchased from Tamura Corporation, Japan. Approximately 0.05 g of copper iodide (γ-CuI) powder (purity ~ 95%), purchased from Wako Pure Chemical Industries Ltd., was evaporated for 2 min in a vacuum chamber at a pressure of ~ 10^{-3} Pa and an applied current of 35 mA. The thickness of the γ-CuI layer was controlled by varying the deposition duration. Metal electrodes were deposited on the fabricated γ-CuI/β- Ga_2O_3 heterostructure to complete the device structure. Gold (Au) and indium (In) electrodes were deposited on top of the γ-CuI and backside of the β- Ga_2O_3, respectively, using a metal shadow mask with a thermal evaporator instrument under a high vacuum (~ 10^{-3} Pa). The CuI/β– Ga_2O_3 heterostructure samples were characterized using X-ray diffraction (XRD), UV–Vis absorption spectroscopy, and Raman spectroscopy. XRD studies were carried out using a Rigaku Smart Lab SE with Cu Kα radiation as the X-ray source (λav = 1.5406 Å). The surface of the heterostructure was analyzed using a JEOL JSM 5600 scanning electron microscope (SEM) at an accelerating voltage of 20 kV. Raman spectroscopy measurements on the β- Ga_2O_3 and deposited CuI film were performed using an NRS 3300 laser Raman spectrometer at a laser excitation wavelength of 532.08 nm. UV–Vis absorption spectroscopy analysis was performed using a JASCO V-670 K spectrophotometer. The CuI film and Au and In metal electrodes were deposited using a ULVAC VPC-260F thermal evaporator. Current density–voltage (J–V) measurements were carried out using a two-probe system and a Keithley 2401 source meter at different device temperatures. The J–V characteristics of the heterostructure were analyzed at different temperatures (298–473 K) on a hot plate using a digital temperature controller.

3.3 Results and discussion

Figure 3.1(a) shows the XRD spectra of the β- Ga_2O_3 substrate and the fabricated γ-CuI/β- Ga_2O_3 heterostructure. A strong diffraction peak at 61.01° corresponding to the (020) reflection phase of β-Ga_2O_3 is observed in both samples. Again, an additional high-intensity peak is observed at 26.06° corresponding to the (111) plane of the cubic-phase γ-CuI for the γ-CuI/β-Ga_2O_3 heterostructure sample, which is in accordance with the JCPDS Card number 06-0246 [24,25]. The predominantly (111)-oriented cubic-phase γ-CuI is obtained on the monoclinic β-Ga_2O_3 single-crystal substrate, which is consistent with previously reported results. [21,22].

Figure 3.1(b) shows the Raman scattering spectra of the single-crystal β-Ga_2O_3 substrate and the γ-CuI/β-Ga_2O_3 heterostructure. The low-frequency Raman peaks at 146, 17, and 201 cm^{-1} denote the liberation and translation of the tetrahedral/octahedral chains. The mid-frequency Raman peaks at 348, 417, and 476 cm^{-1} are related to the distortion of the Ga_2O_6 octahedra. The high-frequency Raman peaks at 631, 654, and 767 cm^{-1} indicate the stretching and bending of the GaO_4 tetrahedra. The high-intensity A_g Raman mode at 200 cm^{-1} signifies the high-quality crystalline nature of the β-Ga_2O_3 sample used for the device fabrication [20]. Further, by analyzing the Raman spectra of the fabricated heterostructure, we observed an additional peak at 119 cm^{-1}, corresponding to the deposited γ-CuI film on the β-Ga_2O_3 substrate. The XRD spectra of the β-Ga_2O_3 substrate and the γ-CuI/β-Ga_2O_3 sample can be correlated with the Raman analysis of the purity and crystalline nature of the prepared samples for the device fabrication.

Figure 3.1(c) shows the UV absorption spectra of the γ-CuI film deposited on a glass substrate in comparison to the absorption spectra of β-Ga_2O_3. The γ-CuI film shows absorption peaks in the range of 350–400 nm, whereas the absorption for the β-Ga_2O_3 sample is obtained in the range of 190–280 nm. Thus, the bandgap width for the γ-CuI/β-Ga_2O_3 heterojunction is 190-400 nm.

Figure 3.1(d) shows the Tauc plot for calculating the optical bandgap of the deposited γ-CuI film, which is computed as 3.02 eV, consistent with previously reported values [26]. A Tauc plot of the β-Ga$_2$O$_3$ sample was plotted for comparison with the Tauc plot of the γ-CuI film. The optical band gap of β-Ga$_2$O$_3$ was computed as 4.6 eV, which agrees with the theoretical value. [1,27] Furthermore, the optical absorption study and the obtained bandgap can be correlated with the highly crystalline β-Ga$_2$O$_3$ and γ-CuI/β-Ga$_2$O$_3$ heterostructure samples, as observed from the Raman and XRD analyses.

Figure 3.1(e) shows the SEM image of the thermally evaporated γ-CuI film on β-Ga$_2$O$_3$. The thermally evaporated γ-CuI film on β-Ga$_2$O$_3$ showed a granular morphology, where the grain size of the γ-CuI and surface roughness may change with the deposition conditions.

Figure 3.1(f) shows a tilted SEM image of the γ-CuI film on β-Ga$_2$O$_3$, presenting the thickness of γ-CuI around 1µm. The thickness and uniformity of the film on the β-Ga$_2$O$_3$ substrate were controlled by the evaporation rate, where the thickness and uniformity of the γ-CuI film can significantly differ with the deposition rate. A heterojunction device was fabricated with the as-deposited γ-CuI film, where a persistent diode characteristic was obtained, as discussed next, with a device structure of Au/γ-CuI/β-Ga$_2$O$_3$/In.

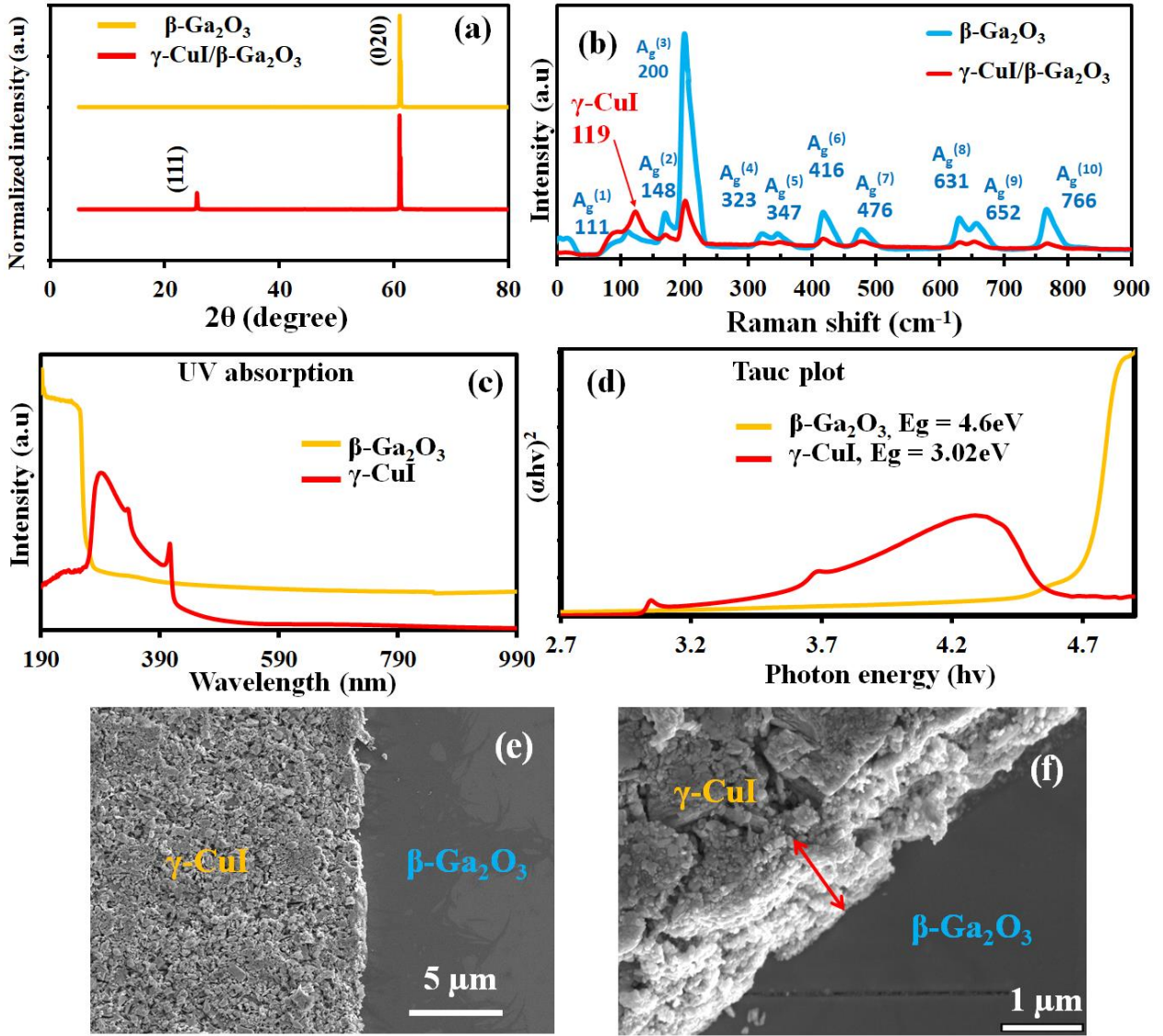**Figure 3.1.** (a) X-ray diffraction pattern of the β-Ga₂O₃ substrate and γ-CuI/β-Ga₂O₃ heterostructure (b) Raman spectra of the β-Ga₂O₃ substrate and γ-CuI film (c) UV absorption of the β-Ga₂O₃ substrate and γ-CuI film (d) Tauc plots, presenting the respective bandgap of the two materials; SEM image of γ-CuI film (e) on top of the β-Ga₂O₃ substrate and (f) a tilted view at the edge of the γ-CuI film on β-Ga₂O₃.
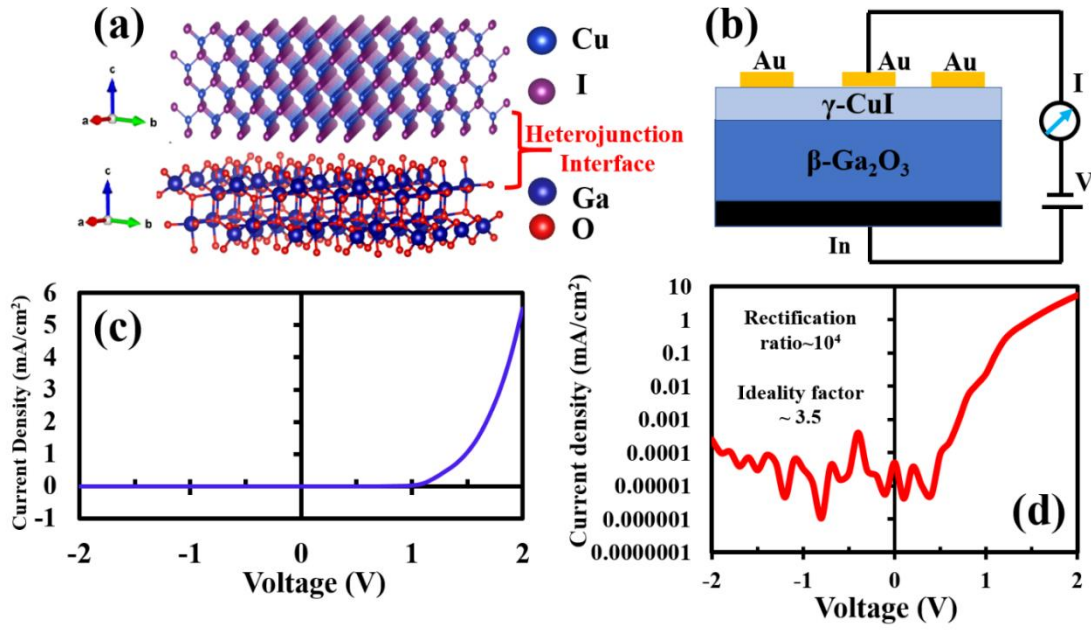
Figure 3.2: (a) cross-section of γ-CuI and β-Ga$_2$O$_3$; (b) schematic heterojunction device of γ-CuI and β-Ga$_2$O$_3$; (c) J–V characteristics; and (d) log plot of the J–V curve of the fabricated device for a voltage range of -2 V to 2 V

Figure 3.2 (a) shows the cross-section stick and ball crystal structure of the γ-CuI and β-Ga$_2$O$_3$ device interface. The electron affinities of the n-type β-Ga$_2$O$_3$ and p-type γ-CuI were in the range of 4.0 and 2.1-2.2 eV, respectively, which indicates the possibility of creating a large build-in field at the interface. The bandgaps of the two materials as calculated from the absorption spectra were 3.02 and 4.6 eV for γ-CuI and β-Ga$_2$O$_3$, respectively. As discussed here, owing to the large differences in the electron affinity and work function, a significant built-in field (φGa$_2$O$_3$-φγ-CuI = V$_{bi}$) can be obtained at the interface of the γ-CuI/β-Ga$_2$O$_3$ heterojunction [18,28]. **Figure 3.2** (b) shows a schematic diagram of the fabricated γ-CuI/β-Ga$_2$O$_3$ vertical heterojunction device. The Au and In electrodes were deposited on γ-CuI and β-Ga$_2$O$_3$, respectively, to fabricate them. The Au electrode was deposited on γ-CuI considering the similar work function in the range of 5.1 eV. A work function in the range 4.08–4.12 eV was selected considering the electron affinity of n-type

β-Ga$_2$O$_3$ to be approximately 4.0 eV [23,29]. The fabricated Au/γ-CuI/β-Ga$_2$O$_3$/In vertical heterojunction device was analyzed for its J–V characteristics. First, the device was analyzed at room temperature (298 K). **Figure 3.2** (c) shows the J–V characteristics at 298 K in the voltage range of –2 V to +2 V under dark conditions. Good rectifying diode behavior was observed with low series resistance and a high rectification ratio (~10^4). **Figure 3.2** (d) shows the log plot of the J–V curve at room temperature. The diode characteristics can be compared with the previously reported results for γ-CuI/β-Ga$_2$O$_3$ and diamond/β-Ga$_2$O$_3$ heterojunction diodes [20,30]. The diode ideality factor (n), computed from the log plot, was found to be 3.5. The diode J–V characteristics can be expressed as follows, correlating the current and voltage with the ideality factor.

$$J = J_0 \left(e^{\frac{qV}{nkT}} - 1 \right),$$
(1)

where J is the current density flowing through the diode, V is the voltage across the diode, J_0 is the saturation current density, T is the temperature in Kelvin, q is the electron charge, and k is the Boltzmann's constant. The n value determines the deviation from the ideal diode owing to the presence of a tunnelling component and barrier inhomogeneity [31]. The ideality factor was higher than some of the previously reported values for β-Ga$_2$O$_3$ heterojunction devices [15,21,22,30,32-35]. In addition, the reverse saturation current was significantly low in the fabricated device, as can be observed from the J–V characteristics. Thus, the deposited γ-CuI on β-Ga$_2$O$_3$ is suitable for the fabrication of the vertical heterojunction device. Subsequently, we analyzed the temperature-dependent J–V characteristics to understand the current transport behaviour at the heterojunction interface.
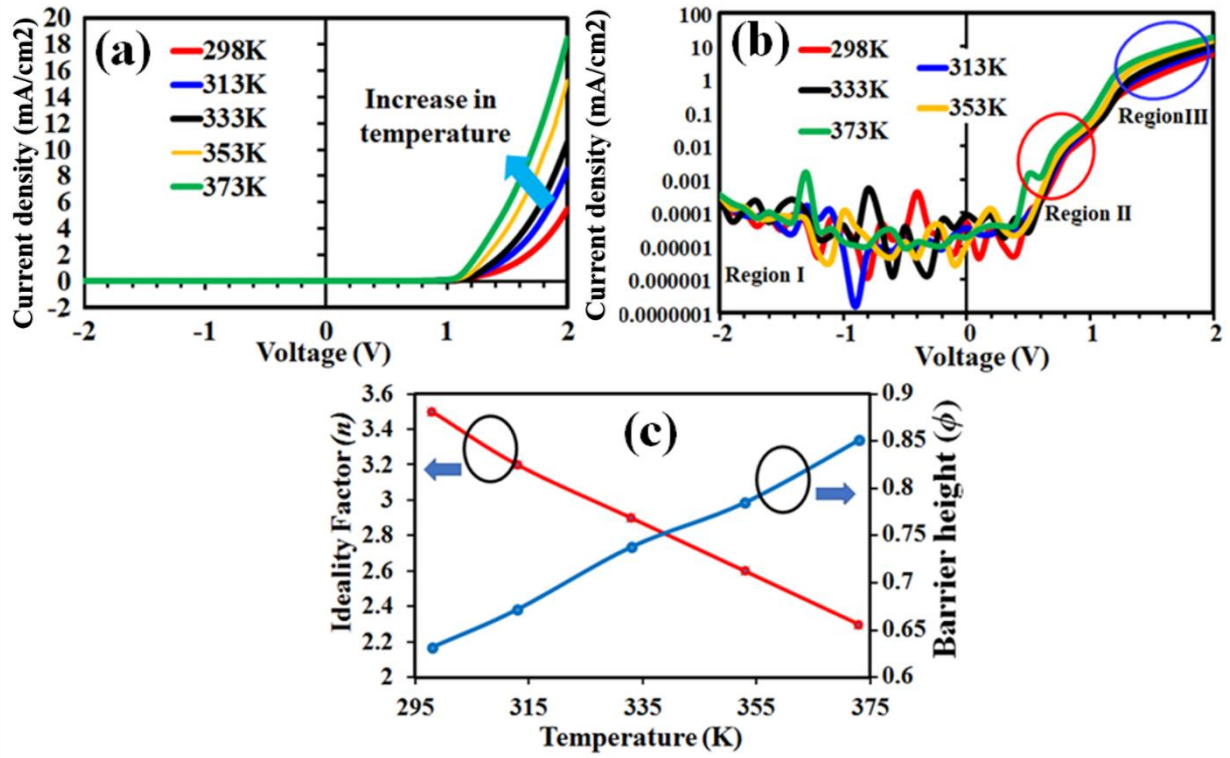
Figure 3.3: (a) J–V characteristics in the temperature range 298–373 K and voltage range of –2 to 2 V; (b) Logarithm representing the current transport behavior (c) Variation in the ideality factor (n) and barrier height (φ) with an applied temperature in the range 298–373 K

Figure 3.3 (a) shows the temperature-dependent J–V characteristics of the Au/γ-CuI/β-Ga$_2$O$_3$/In heterojunction under an applied bias voltage of –2 to +2 V in the temperature range 298–373 K. The temperature-dependent analysis of the γ-CuI/β-Ga$_2$O$_3$ heterostructure elucidated the interface properties and compatibility of the material system for device fabrication. The fabricated device showed consistent rectification diode characteristics as the temperature was increased to 373 K. **Figure 3.3** (b) shows the log plot with an increasing temperature. The forward current consistently increased with an increase in temperature **Figure 3.3** (a); however, the change in current was not significantly high, because the variation in the logarithm plot was not noticeably visible. The

56

saturation current is significantly low, because of which a small change in current is pronounced in the logarithm plot in the reverse bias voltage. The reverse saturation current was slightly non-saturated at the reverse bias voltage for the measured temperature range. This can be attributed to the barrier inhomogeneity at the interface of γ-CuI/β-Ga$_2$O$_3$. Subsequently, the barrier height (φ_B) was analyzed by changing the temperature for the J-V characteristic using the reverse saturation current density equation.

$$J_0 = \mathrm{A}A^*T^2 Exp\left(\frac{-q\phi_B}{kT}\right), \tag{2}$$

where A^* is Richardson's constant (41 A cm^{-2} K^{-2} for β-Ga$_2$O$_3$), A is the contact area, q is the electron charge, T is the temperature in Kelvin, k is the Boltzmann constant, and φ_B is the effective barrier height.

Figure 3.3 (c) shows the trends in n and φ_B at various temperatures. n decreased and φ_B increased as the temperature increased from 298 K to 373 K. The φ_B at the interface between γ-CuI and β-Ga$_2$O$_3$ was approximately 0.632 eV at room temperature (298 K) from the J–V characteristics, which is relatively higher than those of other β-Ga$_2$O$_3$ heterojunction devices. However, the measured barrier height was smaller than the theoretical value, as mentioned earlier, which may be due to the presence of a tunneling component at the heterojunction interface in the presence of the interface states [24].
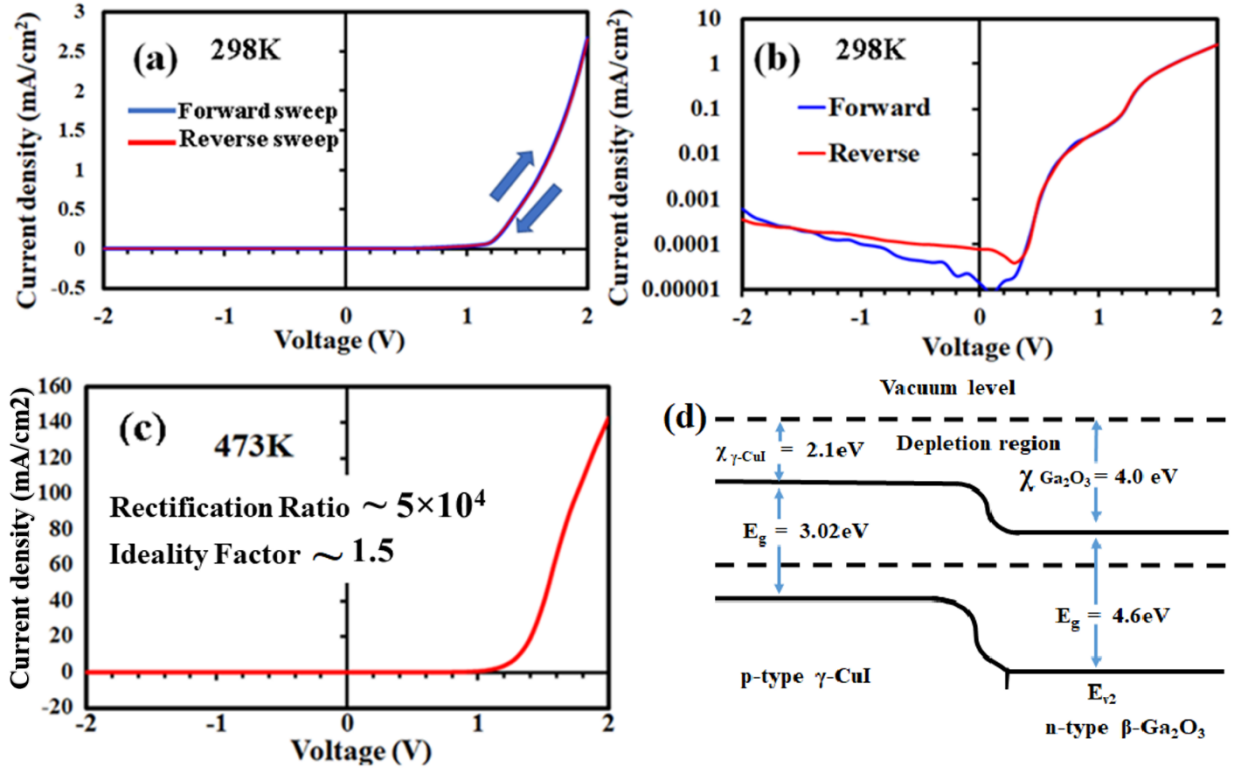
Figure 3.4: (a) J–V characteristics for the forward and reverse sweep of bias voltage; (b) Log plot of the J–V curve at room temperature (298 K); (c) J–V characteristics of the Au/γ-CuI/β-Ga$_2$O$_3$/In heterojunction device at a significantly higher temperature of 473 K with excellent rectification characteristics; and (d) energy bandgap diagram of the γ-CuI/β-Ga$_2$O$_3$ heterojunction device in equilibrium

Furthermore, the interface quality of the Au/γ-CuI/β-Ga$_2$O$_3$/In heterojunction was investigated. The J–V characteristics of the forward and reverse sweeps were measured to analyze the occurrence of electrical hysteresis under dark conditions. **Figure 3.4** (a) shows the forward and reverse sweeps under a bias voltage of +2 V. The measured J–V curve showed no hysteresis effect for the forward bias voltage. **Figure 3.4** (b) shows the logarithmic plot of the J–V characteristics with a small electrical hysteresis in the reverse saturation current. As the reverse saturation current

is much smaller, the electrical hysteresis becomes more prominent. The presence of electrical hysteresis in the reverse saturation current indicates some level of interface states for the fabricated γ-CuI/β-Ga$_2$O$_3$ heterojunction [29,31]. **Figure 3.4** (c) shows the J–V characteristics of the fabricated device at 473 K, which still showed excellent rectification diode characteristics at a rectification ratio of 10^2. Further, the J–V characteristic was also measured at 523 K; however, the device properties were not consistent, as a dark color appeared around the Au electrode due to oxidation. The study of the high-temperature stability of the γ-CuI/β-Ga$_2$O$_3$ device is an important aspect to confirm the suitability of the fabricated heterojunction device. **Figure 3.4** (d) shows the probable energy band diagram for the γ-CuI/β-Ga$_2$O$_3$ heterojunction device at equilibrium. The energy band diagram was configured from the electron affinity and bandgap values of n-type β-Ga$_2$O$_3$ (χ = 4.0 eV; E$_g$ = 3.02 eV) and p-type γ-CuI (χ = 2.1~2.2 eV; E$_g$ = 4.6 eV). Because the electron affinities of the two semiconductors are significantly different, a large band bending as well as a large barrier potential at the heterojunction interface can be estimated. [24,36,37,38]. The band diagram also represents the suitability of both the semiconductors for heterojunction device applications, where the formation of an interface with the deposition process can significantly affect the device performance. From the temperature-dependent analysis, it can be observed that the γ-CuI/β-Ga$_2$O$_3$ heterojunction is quite stable with consistent highly rectifying diode characteristics. Most importantly, the experimental results suggest that the observed barrier inhomogeneity from the temperature-dependent J–V analysis can be correlated with the electrical hysteresis of the diode characteristics, which signifies the presence of surface defects and interface states.

3.4 Conclusion

We investigated the temperature-dependent device characteristics of the p-type γ-CuI and n-type β-Ga2O3 heterojunctions, thereby analyzing the interface properties. A predominantly (111)-oriented cubic-phase γ-CuI was deposited on a β-Ga2O3 substrate by evaporation. The fabricated γ-CuI/β-Ga2O3 heterojunction showed excellent diode characteristics with a high rectification ratio and low reverse saturation current at 298 K, in the presence of a large barrier height of 0.632 eV. A decrease in the ideality factor and an increase in barrier height were observed when the temperature was increased from 298 to 373 K, indicating a barrier inhomogeneity at the heterojunction interface due to the surface defects present there. The electrical analysis also showed a small hysteresis effect on the reverse saturation current for the fabricated γ-CuI/β-Ga2O3 heterojunction. The presence of electrical hysteresis for the reverse saturation current and the barrier inhomogeneity in the temperature-dependent.

3.5 Reference

[1] Baldini M, Galazka Z, Wagner G (2018) Recent progress in the growth of β-Ga_2O_3 for power electronics applications. Mater. Sci. Semicond. Process 78: 132-146

[2] Chabak KD, McCandless JP, Moser NA, Green AJ, Mahalingam K, Crespo A, Hendricks N, Howe BM, Tetlak SE, Leedy K, Fitch RC, Wakimoto D, Sasaki K, Kuramata A, Jessen GH (2018) Recessed-gate enhancement-mode β-Ga_2O_3 MOSFETs. IEEE Electron Device Lett 39: 67-70

[3] Oishi T, Koga Y, Harada K, Kasu M (2015) High-mobility β-Ga_2O_3(201) single crystals grown by edge-defined film-fed growth method and their Schottky barrier diodes with Ni contact. Appl. Phys. Express 8: 031101

[4] Ma N, Tanen N, Verma A, Guo Z, Luo T, Xing HG, Jena D(2016) Intrinsic electron mobility limits in b-Ga_2O_3. Appl. Phys. Lett 109: 212101

[5] Kim M, Seo JH, Singisetti U, Ma Z (2017) Recent advances in free-standing single crystalline wide band-gap semiconductors and their applications: GaN, SiC, ZnO, β-Ga_2O_3, and diamond. Mater. Chem. C, 5: 8338.

[6] Xu J, Zheng W, Hiang F (2019) Gallium oxide solar-blind ultraviolet photodetectors: a review. J. Mater. Chem. C, 7: 8753-8770

[7] Pratiyush AS, Krishnamoorthy S, Muralidharan R, Rajan S, Nath DN (2019) 16 - Advances in Ga_2O_3 solar-blind UV photodetectors, gallium oxide technology, devices and applications, metal oxide 365-399, OSA Publications China.

[8] Higashiwaki M, Murakami H, Kumagai Y, Kuramata A (2016) Current status of Ga_2O_3 power devices, J. Appl. Phys. 55: 1202

[9]   Oshima T, Okuno T, Arai N, Suzuki N, Ohira S, Fujita S (2008) Vertical solar-blind deep-ultraviolet Schottky photodetectors based on β-Ga_2O_3 substrates. Appl. Phys. Express. 1: 011202

[10]   Jia M, Wang F, Tang L, Xiang J, Teng KS, Lau SP (2020) High-performance deep ultraviolet photodetector based on NiO/β-Ga_2O_3 heterojunction Nanoscale Res Lett. 15: 47

[11]   Kim H, Tarelkin S, Polyakov A, Troschiev S, Nosukhin S, Kuznetsov M, Kim J (2020) Ultrawide-bandgap p-n heterojunction of diamond/β-Ga_2O_3 for a solar-blind photodiode. ECS J. Solid State Sci. Technol. 9: 045004

[12]   Farzana E, Zhang Z, Paul PK, Arehart AR, Ringel SA (2017) Influence of metal choice on (010) β- Ga_2O_3 Schottky diode properties. Appl. Phys. Lett. 110: 202102

[13]   Konishi K, Goto K, Murakami H, Kumagai Y, Kuramata A, Yamakoshi S, Higashiwaki M (2017) 1-kV vertical Ga_2O_3 field-plated Schottky barrier diodes. Appl. Phys. Lett. 110: 103506

[14]   Lin R, Zheng W, Zhang D, Zhang Z, Liao Q, Yang L, Huang F (2018) High-performance graphene/β-Ga_2O_3 heterojunction deep-ultraviolet photodetector with hot-electron excited carrier multiplication. ACS Appl. Mater. Interfaces 26: 22419

[15]   Zhang J, Han S, Cui M, Xu X, Li WL, Xu H, Jin C, Gu M, Chen L, Zhang KHL (2020) Fabrication and interfacial electronic structure of wide bandgap NiO and Ga_2O_3 p$-$n heterojunction. ACS Appl. Electron. Mater. 2: 456-463

[16]   Zhuo R, Wu D, Wang Y, Wu E, Jia C, Shi Z, Xu T, Tiana Y, Li X (2018) A self-powered solar-blind photodetector based on a $MoS_2/\beta\text{-}Ga_2O_3$ heterojunction. J. Mater. Chem. C. 6: 10982-10986

[17]   Yamada N, Ino R, Tomura H, Kondo Y, Ninomiya Y (2017) High-mobility transparent p-type CuI semiconducting layers fabricated on flexible plastic sheets: toward flexible transparent electronics. Adv. Electron. Mater. 3 12: 1700298.

[18]   Ranade AK, Pradeep D, Mahyavanshi R, Tanemura M, Kalita G (2019) Formation of effective CuI-GaN heterojunction with excellent ultraviolet photoresponsive photovoltage. Phys. Status Solidi A, 216: 1900200

[19]   Yang C, Knei M, Schein FL, Lorenz M, Grundmann M (2016) Room-temperature domain epitaxy of copper iodide thin films for transparent CuI/ZnO heterojunctions with high rectification ratios larger than 109. Sci. Rep. 6: 21937

[20]   Ayhan ME, Shinde M, Todankar B, Pradeep D, Ranade AK, Tanemura M, Kalita G (2020) Ultraviolet radiation-induced photovoltaic action in $\gamma\text{-}CuI/\beta\text{-}Ga_2O_3$ heterojunction. Mater. Lett. 262: 127074

[21]   Li S, Zhi Y, Lu C, Wu C, Yan Z, Liu Z, Yang J, Chu X, Guo D, Li P, Wu Z, Tang W (2020) Broadband ultraviolet self-powered photodetector constructed on exfoliated β-Ga2O3 /CuI core-shell microwire heterojunction with superior reliability. J. Phys. Chem. Lett. 12: 447–453

[22]   Gallagher JC, Koehler AD, Tadjer MJ, Mahadik NA, Anderson TJ, Budhathoki S, Law KM, Hauser AJ, Hobart KD, Kub FJ (2019) Demonstration of CuI as a p-n heterojunction to β-Ga2O3. Appl. Phys. Express. 12: 104005

[23]   Ranade AK, Mahyavanshi RD, Desai P, Kato M, Tanemura M, Kalita G (2019) Ultraviolet light induced electrical hysteresis effect in graphene-GaN heterojunction. Appl. Phys. Lett.114: 151102

[24]   Fares C, Ren F, Hays DC, Gila BP, Tadjer M, Hobart KD, Pearton SJ (2018) Valence band offsets for CuI on (-201) bulk Ga_2O_3 and epitaxial (010) (Al0.14Ga0.86)2O3. Appl. Phys. Lett. 113: 182101

[25]   Yamada N, Kondo Y, Ino R (2019) Low-temperature fabrication and performance of polycrystalline cui films as transparent p-type semiconductors. Phys. Status Solidi. 216: 1700782

[26]   Yang C, Souchay D, Kneiß M, Bogner M, Wei HM, Lorenz M, Oeckler O, Benstetter G, Fu YQ, Grundmann M (2017) Transparent flexible thermoelectric material based on non-toxic earth-abundant p-type copper iodide thin film. Nat. Commun. 8: 1–7

[27]   Kalita G, Mahyavanshi RD, Desai P, Ranade AK, Kondo M, Dewa T, Tanemura M (2018) Photovoltaic action in graphene-Ga2O3 heterojunction with deep-ultraviolet irradiation. Phys. Status Solidi RRL 1800198

[28]   López I, Nogales E, Hidalgo P, Méndez B, Piqueras J (2012) Field emission properties of gallium oxide micro- and nanostructures in the scanning electron microscope. Phys. Status Solidi. 209: 113-117

[29]   Michaelson HB (1977) The work function of the elements and its periodicity. J. Appl. Phys. 48: 4729-4733

[30]   Kim H, Tarelkin S, Polyakov A, Troschiev S, Nosukhin S, Kuznetsov M, Kim J (2020) Ultrawide-bandgap p-n heterojunction of diamond/β-Ga2O3 for a solar-blind photodiode. ECS J. Solid State Sci. Technol. 9: 045004

[31]   Kalita G, Shaarin MD, Paudel B, Mahyavanshi R, Tanemura M (2017) Temperature dependent diode and photovoltaic characteristics of graphene-GaN heterojunction. Appl. Phys. Lett. 111: 013504

[32]   Fares C, Ren F, Hays DC, Gila BP, Tadjer M, Hobart KD, Pearton SJ (2018) Valence band offsets for CuI on (-201) bulk Ga_2O_3 and epitaxial (010) $(Al0.14Ga0.86)_2O_3$. Appl. Phys. Lett. 113: 182101.

[33]   Zhang, Zheng W, Lin RC, Li TT, Zhang ZJ, Huang F (2018) High quality β-Ga_2O_3 film grown with N_2O for high sensitivity solar-blind-ultraviolet photodetector with fast response speed. J. Alloys Compd. 735: 150–154

[34]   Alonso M, Cimino R, Horn K (1990) Surface photovoltage effects in photoemission from metal-GaP(110) interfaces: Importance for band bending evaluation. Phys. Rev. Lett. 64: 1947–1950

[35]   Woodall JM, Islam MS, Kaya A, Dryden DM, Mao H, Alhalaili B (2017) Oxidation of GaAs substrates to enable β-Ga_2O_3 films for sensors and optoelectronic devices. In: M. Matin, A.K. Dutta, S. Chowdhury (eds.) Wide bandgap power devices appl. II, SPIE, p. 11

[36]   Mohamed M, Irmscher K, Janowitz C, Galazka Z, Manzke R, Fornari R (2012) Schottky barrier height of Au on the transparent semiconducting oxide β-Ga_2O_3. Appl. Phys. Lett. 101: 132106

[37]   Schein FL, Von Wenckstern H, Grundmann M (2013) Transparent p-CuI/n-ZnO heterojunction diodes, Appl. Phys. Lett. 102: 92109.

[38]   Motaung DE, Mhlongo GH, Makgwane PR, Dhonge BP, Cummings FR, Swart HC, Ray SS (2018) Ultra-high sensitive and selective H_2 gas sensor manifested by interface of n–n heterostructure of CeO_2-SnO_2. Sensors Actuat B-Chem 254: 984-995.

[39] Dong, L., Jia, R., Xin, B. et al. Effects of oxygen vacancies on the structural and optical properties of β-Ga2O3. Sci Rep 7, 40160 (2017).

Chapter 4

Characteristics of vertical Ga_2O_3 Schottky junctions with the interfacial hexagonal boron nitride film

4.1 Introduction

Gallium oxide (Ga_2O_3) with an ultra-wide bandgap (UWBG) has piqued the interest of researchers working on deep ultraviolet (UV) photonics and next-generation power electronic devices [1-5]. Semiconductors based on UWBG Ga_2O_3 materials can withstand much higher critical electric fields (6–8 MV/cm) before avalanche breakdown than silicon (Si), silicon carbide (SiC), and gallium nitride (GaN) based devices [1,6,7]. Furthermore, Baliga's figure of merit presents the advantage of Ga_2O_3 for power switching applications over the Si (3000×), SiC (10×), and GaN (4×) [8,9]. It has been demonstrated that high-quality single-crystal Ga_2O_3 can be synthesized using melt growth techniques such as Czochralski, floating zone, and edge-defined film-fed growth (EFG) [10-15]. In addition, halide vapour phase epitaxy (HVPE), molecular beam epitaxy (MBE), and chemical vapour deposition (CVD) methods for growing high-quality Ga_2O_3 have been developed [16-24]. Johnson's figure of merit (JFOM/Power-frequency product) of Ga_2O_3 (3× of GaN) [25, 26] illustrates the potential benefit of using Ga_2O_3 in radio frequency (RF) devices. Chabak et al. have reported on the fabrication of Ga_2O_3 MOSFET device using a thin and highly doped channel and achieving a drain-source current of 275 mA/mm at a drain to source bias of 10 V for that exhibited record-high f_t/f_{max} = 5.1/17.1 GHz [27]. However, it is expected that Ga_2O_3 devices will suffer from self-heating due to the poor thermal conductivity of the material. The device model demonstrates that a homo-epitaxial device suffers from an unacceptable junction temperature rise to 1500°C at a power density of 10 W/mm, highlighting the importance of applying device level thermal managements to individual Ga_2O_3 devices [28]. In this case, the

integration of thermal conducting materials with Ga_2O_3-based devices may be critical for achieving dependable device performance.

The heterojunction and Schottky junction-based β-Ga_2O_3 devices are of great interest for the development of high-voltage devices and solar-blind UV photodetectors, considering the intrinsic n-type conductivity of β-Ga_2O_3 in presence of unintentional dopants [25-30]. The conventional Ga_2O_3 Schottky junction devices were studied with metal electrodes such as Au, Pt, and Ni, taking into account the metals' appropriate work function [31-32]. Again, studies on metal-insulator-semiconductor (MIS)-based SBD devices have been conducted, owing to the benefit of lowering the reverse saturation current [33-35]. The MIS-based SBD devices have been fabricated using insulating dielectric materials, such as SiO_2, Si_3N_4, and Al_2O_3, etc. [34-36]. The thermal stability of Ga_2O_3 Schottky contacts is also an important aspect, for which materials with high melting temperatures and low reactivity with Ga_2O_3 are of significant interest [37]. Furthermore, controlling near-surface ion damage during sputtering deposition of a barrier layer/insulating dielectric [7] is required. In this case, the CVD synthesized chemically inert insulating hBN layer will be significant with much higher in-plane thermal conductivity for use in Ga_2O_3-based Schottky junctions.

Previously, we have demonstrated the integration of highly conducting graphene and copper iodide (γ-CuI) films with the β-Ga_2O_3 substrate for the fabrication of deep-UV photoresponsive devices [38,39]. Fabrication of quasi-two-dimensional metal-insulator-semiconductor field-effect transistors was demonstrated by the mechanical transfer process of hBN and nano thin flakes β-Ga_2O_3 [40]. In contrast to previous reports, we show how to make a vertical Ni/ β-Ga_2O_3 Schottky junction with and without the hBN interfacial layer. The UWBG heterostructure of hBN and β-Ga_2O_3 can be significant due to the complementing electronic, chemical, and thermal properties of the materials. The following sections go over the specifics of hBN integration with the free-

standing β-Ga$_2$O$_3$ substrate and the fabrication of a vertical Schottky junction. We discovered that the hBN interfacial film can be used to control the device's turn-on voltage and current density.

4.2 Materials and Methods

The hBN film was synthesized on recrystallized Cu (111) foil by the atmospheric pressure CVD (APCVD) as reported previously by the research group [41-43]. For this experiment, ammonia borane (10 mg) is used as a precursor and placed atop a magnetic boat, which was placed inside the tube about 20 cm away from the furnace to avoid precursor loss before the deposition step. The furnace was set at a high temperature of 1050°C for the growth of the hBN film on the Cu surface. During the deposition step, the gas flow into the chamber was changed by the addition of argon gas with a flow rate of 98 sccm and flow rate of hydrogen gas was reduced to 2 sccm and once the mixed gas flow of 98:2 of Ar: To achieve vaporization of ammonia borane, the precursor is brought close to the furnace using a magnet at 3 cm away from the furnace. The deposition step was set for 40 min, allowing for the formation of an hBN layer on a Cu (111) substrate. Finally, the cooling step was completed by simultaneously switching the H$_2$ gas flow, partially opening the furnace, and moving the precursor approximately 20 cm away from the furnace to avoid a secondary deposition. After the reaction chamber was cooled to room temperature, the hBN grown Cu foil was removed and subjected to a wet transfer process as described in previous reports. [40]. A hBN/β-Ga$_2$O$_3$ stack was obtained by transferring the CVD synthesized hBN film on the Ga$_2$O$_3$ substrate. The fabricated hBN/β-Ga$_2$O$_3$ stack was used to fabricate an MIS-based Schottky junction device by depositing Ni and In metal electrodes. The fabricated Schottky junction with a configuration of Ni/hBN/β-Ga$_2$O$_3$/In was characterized and the effect of the interfacial hBN layer was analyzed.

The as-received β-Ga$_2$O$_3$ sample was characterized using X-ray diffraction (XRD), UV-Vis absorption spectroscopy, and Raman spectroscopy. The XRD studies were carried out using a Rigaku Smart Lab SE with Cu Kα radiation as the X-ray source (λ_{av} = 1.5406 Å). A JEOL JSM 5600 scanning electron microscope (SEM) at a voltage of 20 kV was used to examine the hBN transferred β-Ga$_2$O$_3$ sample. An NRS 3300 laser Raman spectrometer was used to analyze the β-Ga$_2$O$_3$ sample at a laser excitation wavelength of 532.08 nm. Vertical Schottky junction devices were created by depositing Ni and In metal electrodes with the help of a metal mask. Metal mask with round-shaped holes (electrode area ~0.003 cm^2) was used to deposit the top Ni electrode, whereas In electrode was deposited on the backside of the β-Ga$_2$O$_3$ substrate almost covering the entire surface. The metal electrodes were deposited by using the ULVAC VPC-260F thermal evaporator under a high vacuum. The current density-voltage (J-V) measurements were carried out using a two-probe system and a Keithley 2401 source meter at room temperature. The deep-UV illumination measurement was performed using a UV lamp of 254 nm wavelength and light intensity of 614 μW/cm^2.

4.3 Results and discussion

Figure 4.1 (a) shows the cross-sectional image of the hBN and β-Ga$_2$O$_3$ heterostructure with Schottky junction. A barrier layer for the β-Ga$_2$O$_3$ Schottky junction can be formed by an hBN layer with a high bandgap (6.0 eV) and a suitable dielectric constant. The XRD spectra of the free-standing β-Ga$_2$O$_3$ substrate are shown in **Figure 4.1**(b) A strong diffraction peak at 61.01° corresponding to the (020) reflection phase of β-Ga$_2$O$_3$ was observed for the sample. The XRD spectra are by the JCPD card number 06-0246 [38]. **Figure 4.1** (c) shows an SEM image for the transferred hBN layer on the β-Ga$_2$O$_3$ substrate.
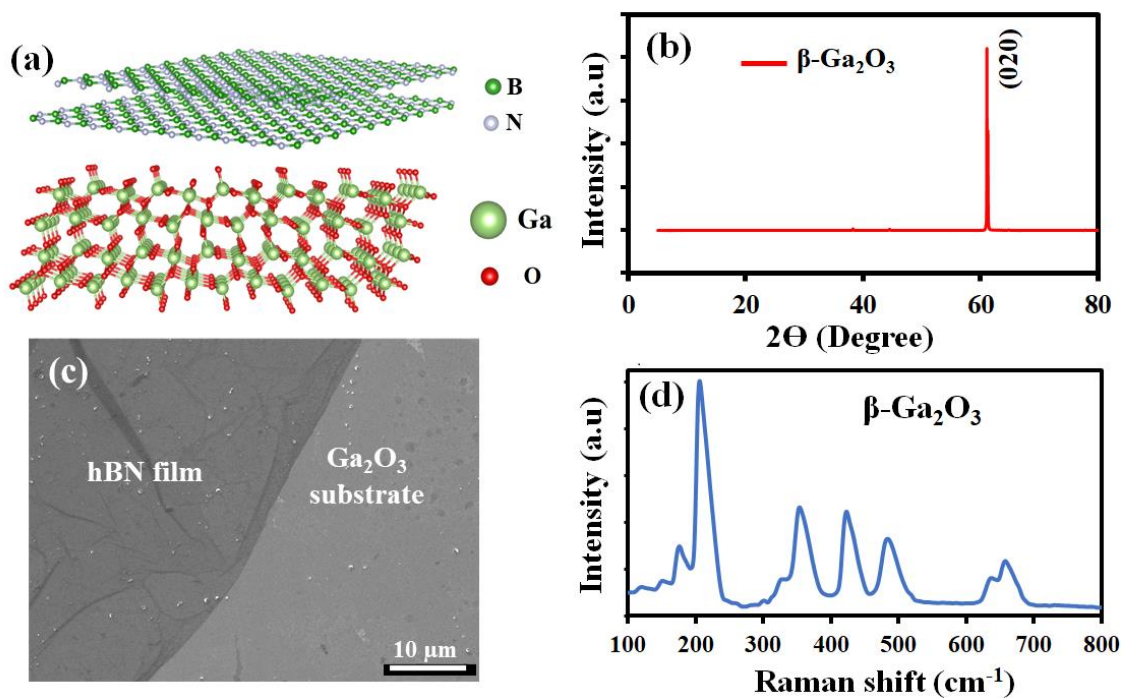
Figure 4.1: (a) Cross-section schematic diagram of hBN and β-Ga$_2$O$_3$ heterostructure. (b) X-ray diffraction pattern of the free-standing β-Ga$_2$O$_3$ substrate. (c) SEM image of hBN film on the β-Ga$_2$O$_3$ substrate. (d) Raman spectra of the β-Ga$_2$O$_3$ sample.

The transferred hBN film on β-Ga$_2$O$_3$ substrate remains intact due to van-der-Waals interaction; however, SEM analysis revealed the formation of a wrinkle in the hBN thin film as well as surface impurities. The Raman spectra of the β-Ga$_2$O$_3$ sample are shown in **Figure 4.1**(d), with a high-intensity Raman peak at 200 cm^{-1} for Ag Raman mode, indicating the high-quality crystalline nature of the β-Ga$_2$O$_3$ sample used for device fabrication. The mid and high-frequency Raman peaks at around 354 cm^{-1}, 424 cm^{-1}, 486 cm^{-1}, 640 cm^{-1}, and 657 cm^{-1}, corresponding to distortion of Ga$_2$O$_6$ octahedra and the stretching/bending of the GaO$_4$ tetrahedra, respectively, as also discussed in previous reports [42]. These analyses show a successful transfer of the CVD synthesized hBN film on the bulk β-Ga$_2$O$_3$ substrate. The hBN/β-Ga$_2$O$_3$ sample was further studied by XPS analysis.
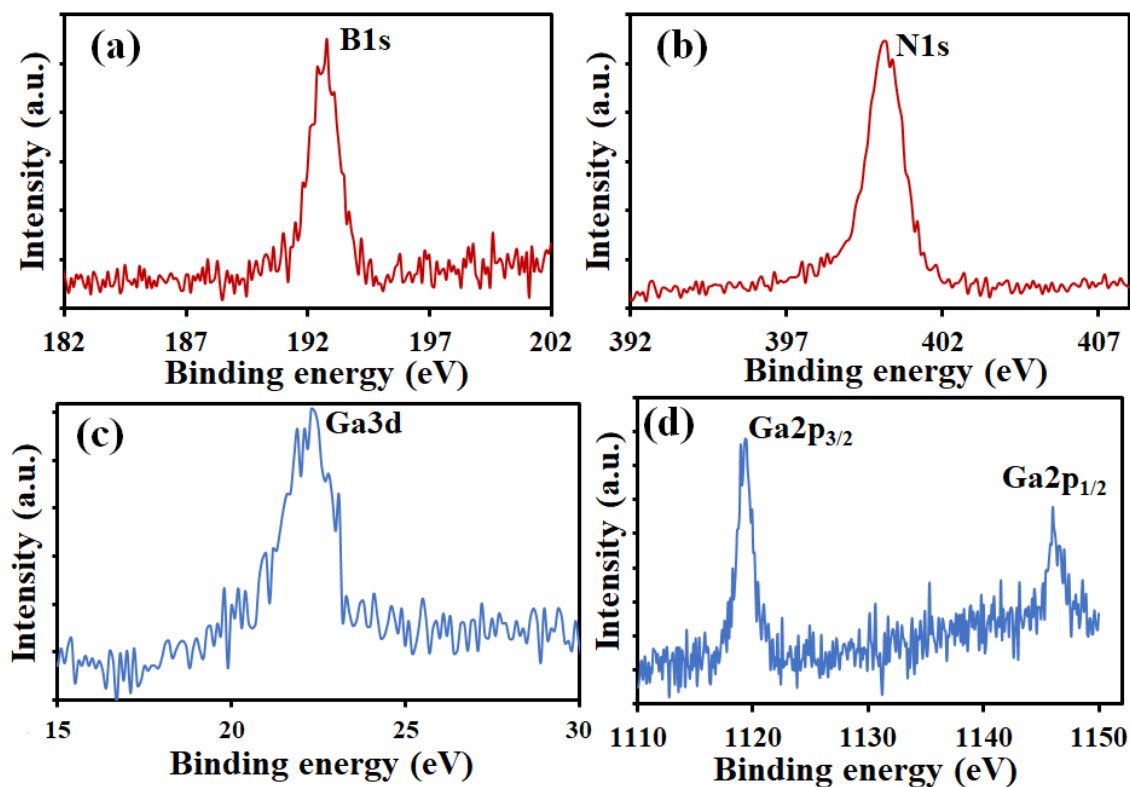
Figure 4.2: XPS spectra for the fabricated hBN/β-Ga$_2$O$_3$ heterostructure sample. a) B1s spectra with a peak center at around 192.8 eV, (b) N1s spectra with a peak center at 400.1 eV, (c) Ga3d spectra with a peak center at 22.3 eV, (d) Ga2p$_{3/2}$ and Ga2p$_{1/2}$ peaks with peak centers at 1119.4 and 1146.0 eV.

Figure 4.2 shows the XPS analysis for the hBN/β-Ga$_2$O$_3$ sample, presenting the elemental composition. **Figure 4. 2** (a) shows the B1s XPS spectrum for the hBN/β-Ga$_2$O$_3$ heterostructure with a peak centre at 192 eV. Similarly, **Figure 4.2** (b) shows the N1s XPS spectra for the hBN film on a β-Ga$_2$O$_3$ substrate with a peak centre at 400.1 eV. Again, **Figure 4.2** (c) shows the Ga 3d peak with a peak centre at around 22.3 eV for the β-Ga$_2$O$_3$ sample. The XPS peak for the β-Ga$_2$O$_3$ was obtained considering the thin hBN film for the fabricated hBN/β-Ga$_2$O$_3$ heterostructure. **Figure 4.2** (d) shows the split Ga2p peaks, where Ga2p$_{1/2}$ and Ga2p$_{3/2}$ peaks are obtained at 1119 and 1144.8 eV, respectively. The chemical structures of the hBN/β-Ga$_2$O$_3$ heterostructure were

confirmed by XPS analysis, with the transferred CVD synthesized hBN film remaining intact and stable on the β-Ga$_2$O$_3$ substrate surface. The current-voltage properties of the hBN/β-Ga$_2$O$_3$ heterostructure Schottky junction were studied.
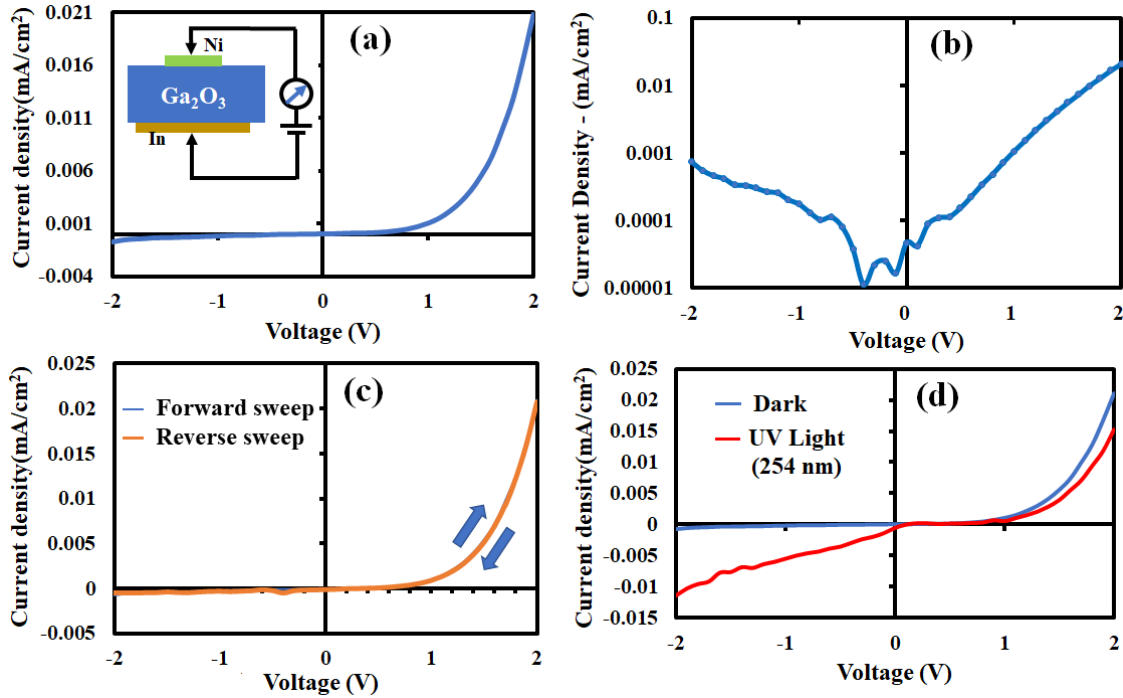

Figure 4.3: J-V characteristic of Ni/ β-Ga$_2$O$_3$/In Schottky junction (a) J-V characteristic for the voltage range of 2 to −2 V (inset shows a schematic diagram of the fabricated device) (b) log plot of the J-V curve. (c) J-V characteristics of the forward and reverse sweep for the voltage range of 2 to −2 V. (d) J-V curve under dark and deep-UV illumination (254 nm).

 Figure 4.3 (a) shows the J-V characteristics for the device with a voltage range of −2 to 2 V. Inset of shows the schematic diagram for the fabricated Ni/β-Ga$_2$O$_3$/In Schottky junction device. **Figure 4.3** (b) shows the logarithmic plot for the J-V characteristics. The J-V characteristics indicate that a suitable Schottky junction formation for the Ni/β-Ga$_2$O$_3$ contact has occurred. **Figure 4.3** (c) depicts the forward and reverse sweeps with a bias voltage ranging from −2 to 2 V. For the forward

bias voltage, the measured J-V curve revealed no hysteresis effect. **Figure 4.3** (d) depicts the J-V characteristics with and without deep-UV light illumination (254 nm). The dark current of 0.00074 mA/cm^2 was enhanced to 0.0115 mA/cm^2 at a reverse bias voltage of 2V, under the illumination of 254 nm wavelength and power of 614 µW/cm^2. The photoresponsivity of Ni/β-Ga$_2$O$_3$/ was calculated. At a reverse bias voltage of 2 V, the current density in a Schottky junction device is 16.28 mA/W. At lower bias voltages, the photoresponsivity of the fabricated device is not considered high; however, the photo responsivity increases with increasing reverse bias voltage [44].
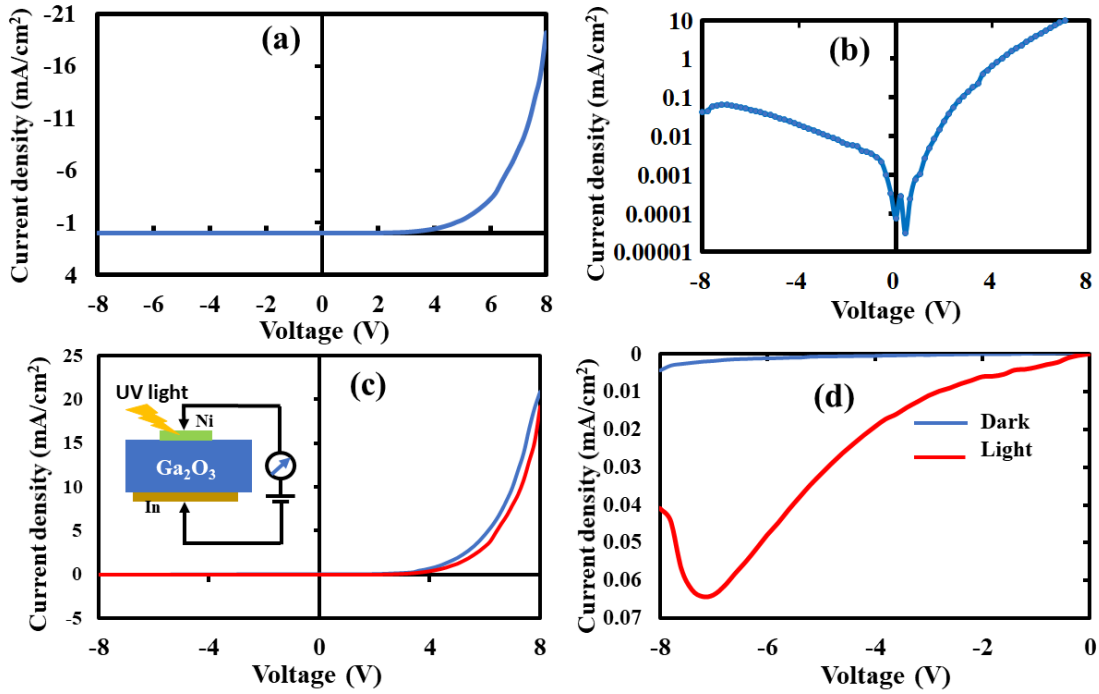
Figure 4.4: J-V characteristic of Ni/β-Ga$_2$O$_3$ 8 to −8 V (a) J-V characteristics of forwarding bias voltage. (b) log plot of J-V curve (c) J-V characteristics of the forward and reverse sweep of bias voltage. (d) log plot of J-V curve dark and UV light at 254 nm.

Figure 4.4 shows the J-V characteristics of the fabricated device with and without UV light illumination under −8 to 8 V. The forward turn-on voltage for the Ni/β-Ga$_2$O$_3$/In Schottky junction

was obtained to be around 3.8 V. **Figure 4.4** (a) and (b) shows the J-V characteristic in the dark and the corresponding logarithmic plot for bias voltages ranging from −8 to 8 V. the J-V characteristics of the Ni/β-Ga$_2$O$_3$ Schottky junction **Figure 4.4** (c) depicts a schematic of the fabricated device with a device structure of Ni/β-Ga$_2$O$_3$In the forward and reverse sweeps at bias voltages ranging from −8 to 8 V. For the forward bias voltage, the measured J-V curve revealed no hysteresis effect. **Figure 4.4** (d) depicts the J-V characteristics of an applied bias voltage ranging from −8 to 8 V under deep ultraviolet illumination (254 nm). Similarly, the dark current of 0.00208 mA/cm^2 was enhanced to 0.0643 mA/cm^2 at a reverse bias voltage of 7.2 V, under the illumination of 254 nm wavelength and power density of 614 μW/cm^2. The photoresponsivity is calculated to be 101.33 mA/W at 7.2 V reverse bias voltage for the constructed Ni/β-Ga$_2$O$_3$/In Schottky junction device.
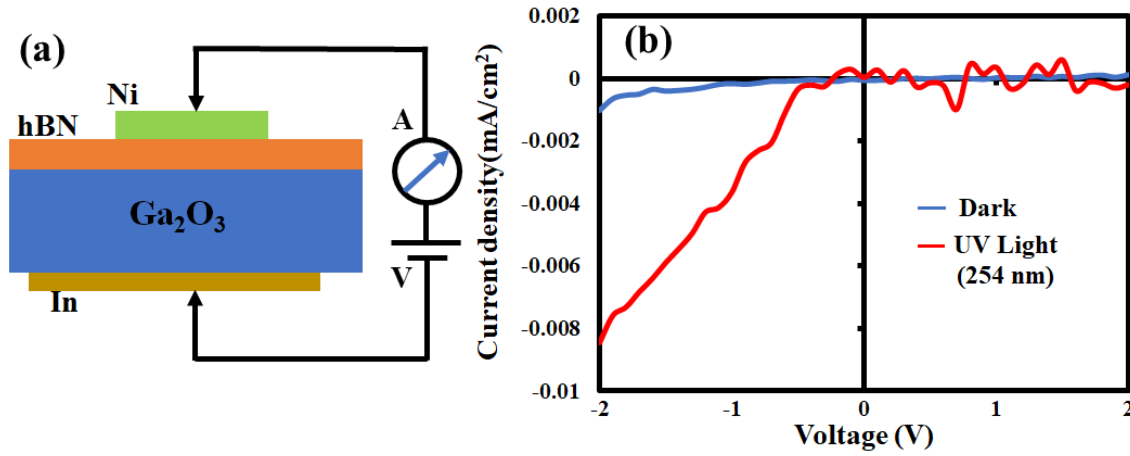
Figure 4.5: (a) Schematic diagram of fabricated Ni/hBN/β-Ga$_2$O$_3$/In Schottky junction. (b) Current density-voltage (J-V) characteristics of the device for a voltage range of 2 to −2 V.

 Figure 4.5 (a) shows a schematic diagram of the fabricated Ni/hBN/β-Ga$_2$O$_3$/In heterojunction Schottky junction device. The CVD synthesized hBN film was transferred on β-Ga$_2$O$_3$ by wet etching the Cu foil with a support layer of PMMA. The Ni top electrode on hBN/β-Ga$_2$O$_3$

heterojunction was deposited by thermal evaporation to configure a Schottky junction device. **Figure 4.5** (b) depicts the J-V characteristics of the fabricated device with and without deep-UV light illumination for a bias voltage range of −2 to 2 V. (wavelength 254 nm). In contrast to the device fabricated without the hBN layer, the forward current did not increase as the bias voltage was increased up to 2 V. At the reverse bias voltage, photoresponsivity was measured, indicating the heterojunction device's sensitivity to deep-UV light.
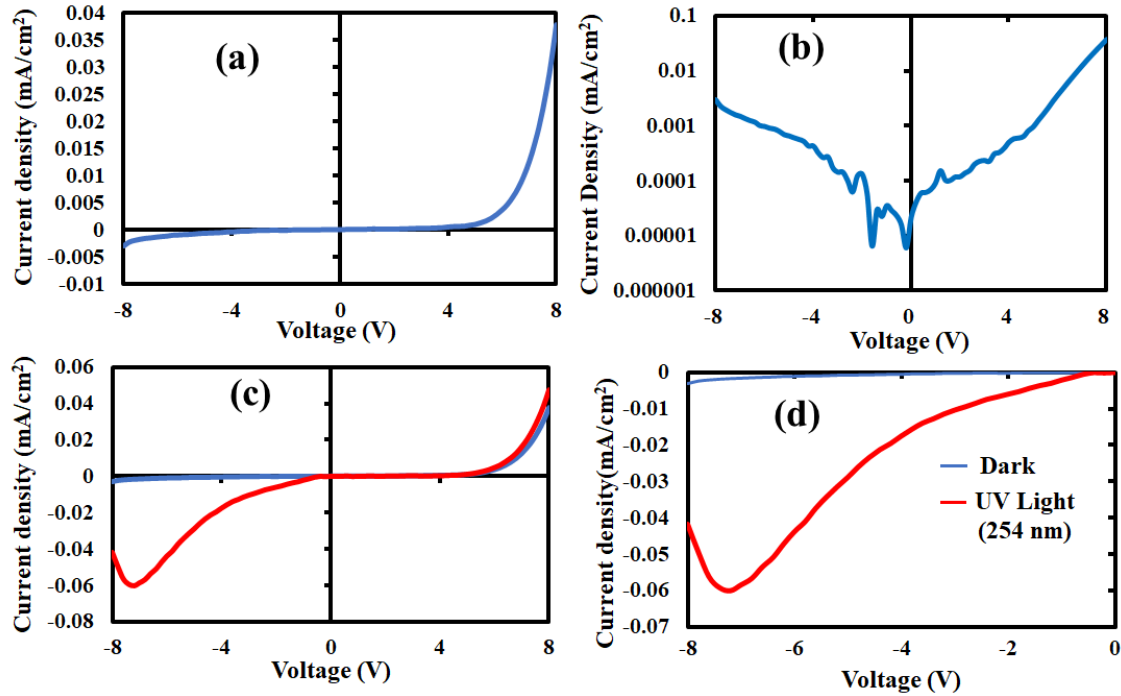
Figure 4.6: (a) J-V characteristics of the Ni/hBN/β-Ga$_2$O$_3$/In Schottky junction device for the voltage range of −8 to 8 V, (b) log plot of the J-V curve. (c) J-V characteristics with and without deep-UV illumination (254 nm) for bias voltage in the range of −8 to 8 V (d) photoresponsivity at the reverse bias voltage (photoresponsivity of 95.11 mA/W at 7.2 V.

 Figure 4.6 (a) shows the J-V characteristics of the Ni/hBN/β-Ga$_2$O$_3$/In Schottky junction device for the voltage range of −8 to 8 V. The forward turn voltage for the Ni/hBN/β-Ga$_2$O/In Schottky junction was obtained to be around 4.8 V, which is higher than the device with hBN layer. As also

observed that the device forward current was significantly low up to an applied voltage of 2 V.

Figure 4.6 (b) shows the corresponding logarithmic plot for the corresponding J-V curve. Similarly, **Figure 4.6** (c) shows the J-V characteristics for the device with and without the light illumination. Under the illumination of deep-UV light with a wavelength of 254 nm, a significant photoresponsivity can be observed in the reverse bias voltage. **Figure 4.6** (d) depicts the J-V curve in the reverse bias voltage range (0 to −8 V) used to measure photoresponsivity at a bias voltage. At 7.2 V bias, the photoresponsivity was 95.11 mA/W. The photoresponsivity is nearly identical to that of the device without the hBN layer; however, the forward turn-on voltage is higher and the current density is lower. Turn-on voltage and forward current density differ significantly with and without the hBN layer on the β-Ga_2O_3, whereas photoresponsive reverse current density was nearly identical at an applied bias voltage of −7.2 V. Thus, a high photoresponsivity can be obtained in a Ni/hBN/β-Ga_2O_3/In based heterojunction Schottky diode with high forward current turn-on voltage and low current density.
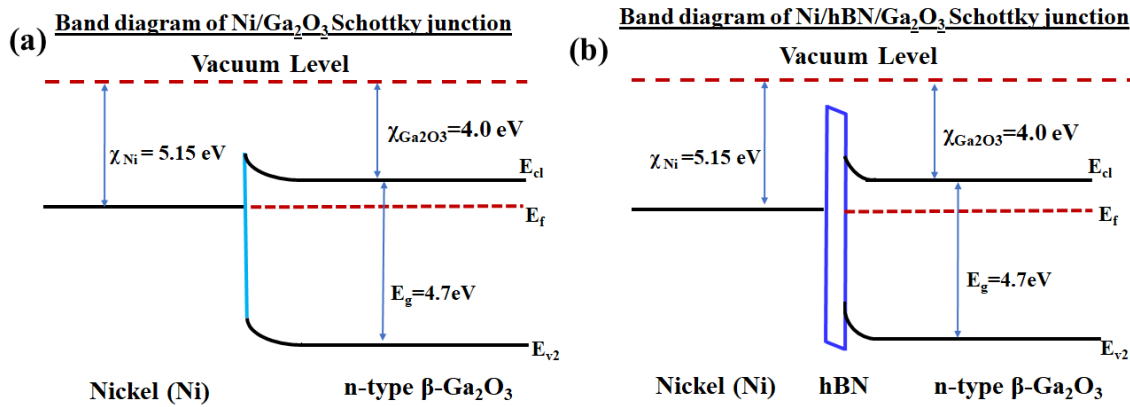

Figure 4.7: (a) Energy band diagram of Ni/β-Ga_2O_3 Schottky junction vacuum level. (b) band diagram of Ni/hBN/β-Ga_2O_3/In Schottky junction vacuum level.

Figure 4.7 (a) shows the energy band diagram for the Ni/β-Ga$_2$O$_3$ Schottky junction. The Ni metal contact with a higher work function (5.15 eV) forms a suitable Schottky potential with the n-type β-Ga$_2$O$_3$. A photoresponsivity was obtained at a reverse bias voltage for the illuminated deep-UV light considering the Schottky junction interface of Ni and Ga$_2$O$_3$. Similarly, **Figure 4.7** (b) shows the energy band diagram for the Ni/β-Ga$_2$O$_3$ Schottky junction, where the hBN layer acts as a barrier layer at the Ni and β-Ga$_2$O$_3$ interface. The J-V curve shows that the diode turn-on voltage increased, but no reduction in reverse saturation current was observed. The photoresponsivity of the Ni/hBN/β-Ga$_2$O$_3$/ Schottky junction to the illuminated deep-UV light of wavelength 254 nm was 95.11 mA/W. Thus, the Ni/hBN/β-Ga$_2$O$_3$/In Schottky junction demonstrated that a significant photoresponsivity can be obtained with a tunable turn-on voltage and forward current.

4.4 Conclusion

In conclusion, we have demonstrated the fabrication of a Ni/β-Ga$_2$O$_3$ Schottky junction device with an hBN interface layer. The hBN film was synthesized by a CVD process and transferred on a free-standing β-Ga$_2$O$_3$ substrate by the wet chemical transfer method. XRD, Raman spectroscopy, and SEM analysis confirmed the hBN/β-Ga$_2$O$_3$ heterostructure of the Ga$_2$O$_3$ substrate and transferred hBN film. The J-V characteristics of a fabricated Schottky junction with and without the hBN interfacial layer were investigated. It was discovered that the hBN interfacial film significantly increases the turn-on voltage for the forward current of the Ni/hBN/Ga$_2$O$_3$/In Schottky junction. Furthermore, the created Ni/hBN/Ga$_2$O$_3$/In Schottky junction showed a photoresponsivity of 95.11 mA/W for the illuminated deep-UV light of wavelength 254 nm. The hBN layer act as a suitable barrier layer as demonstrated, where the turn-on voltage, forward current density, and photo responsivity can be optimized for the Ni/β-Ga$_2$O$_3$ Schottky junction.

4.5 References

1. Tippins, H. H. Optical absorption and photoconductivity in the band edge of β-Ga_2O_3. Phys. Rev. 1965, 140 (1A), A316-A319.

2. Higashiwaki, M.; Sasaki, K.; Kuramata, A.; Masui, T.; Yamakoshi, S. Gallium oxide (Ga_2O_3) Metal-semiconductor field-effect transistors on single-crystal β-Ga_2O_3 (010) Substrates. Appl. Phys. Lett. 2012, 100 (1), 013504.

3. Xue, H. W.; He, Q. M.; Jian, G. Z.; Long, S. B.; Pang, T.; Liu, M. An overview of the ultra-wide bandgap Ga_2O_3 semiconductor-based Schottky barrier diode for power electronics application. Nanoscale Res. Lett. 2018, 13, 1-13.

4. Kalita, G.; Kobayashi, M.; Shaarin, M. D.; Mahyavanshi, R. D.; Tanemura, M. Schottky barrier diode characteristics of graphene-GaN heterojunction with hexagonal boron nitride interfacial layer. Phys. Status Solidi Appl. Mater. Sci. 2018, 215 (18), 1-6.

5. Yikai, L.; Zhaofu, Z.; Zhibin, G.; Qingkai, Q.; Mengyuan, H. Tunable properties of novel Ga_2O_3 monolayer for electronics and optoelectronics applications. ACS Appl. Mater. Interfaces 2020, 12 (27), 30659-30669.

6. Higashiwaki, M.; Sasaki, K.; Murakami, H.; Kumagai, Y.; Koukitu, A.; Kuramata, A.; Masui, T.; Yamakoshi, S. Recent progress in Ga_2O_3 power devices. Semicond. Sci. Technol. 2016, 31 (3).

7. Baldini, M.; Galazka, Z.; Wagner, G. Recent progress in the growth of β-Ga_2O_3 for power electronics applications. Mater. Sci. Semicond. Process. 2018, 78, 132-146.

8. Pearton, S. J.; Ren, F.; Tadjer, M.; Kim, J. Perspective: Ga 2 O 3 for ultra-high power rectifiers and MOSFETS: Ga. J. Appl. Phys. 2018, 124 (22), 220901.

9. Tomm, Y.; Reiche, P.; Klimm, D.; Fukuda, T. Czochralski grown Ga_2O_3 crystals. J. Cryst. Growth 2000, 220 (4), 510-514.

10. Yuan, C.; Zhang, Y.; Montgomery, R.; Kim, S.; Shi, J.; Mauze, A.; Itoh, T.; Speck, J. S.; Graham, S. Modeling and analysis for thermal management in gallium oxide field-effect transistors. J. Appl. Phys. 2020, 127 (15), 154502.

11. Galazka, Z.; Irmscher, K.; Uecker, R.; Bertram, R.; Pietsch, M.; Kwasniewski, A.; Naumann, M.; Schulz, T.; Schewski, R.; Klimm, D.; Bickermann, M. On the bulk β-Ga_2O_3 single crystals grown by the czochralski method. J. Cryst. Growth 2014, 404, 184-191.

12. Aida, H.; Nishiguchi, K.; Takeda, H.; Aota, N.; Sunakawa, K.; Yaguchi, Y. Growth of β-Ga_2O_3 single crystals by the edge-defined, film fed growth method. Jpn. J. Appl. Phys. 2008, 47 (11), 8506-8509.

13. Ohira, S.; Yoshioka, M.; Sugawara, T.; Nakajima, K.; Shishido, T. Fabrication of hexagonal GaN on the surface of β-Ga_2O_3 single crystal by nitridation with NH_3. Thin Solid Films 2006, 496 (1), 53-57.

14. Villora, E. G.; Shimamura, K.; Yoshikawa, Y.; Aoki, K.; Ichinose, N. Large-size β-Ga_2O_3 single crystals and wafers. J. Cryst. Growth 2004, 270 (3-4), 420-426.

15. Kuramata, A.; Koshi, K.; Watanabe, S.; Yamaoka, Y.; Masui, T.; Yamakoshi, S. High-quality β-Ga_2O_3 single crystals grown by edge-defined film-fed growth. Jpn. J. Appl. Phys. 2008, 47 (11), 8506-8509.

16. Nikolaev, V. I.; Pechnikov, A. I.; Nikolaev, V. V.; Scheglov, M. P.; Chikiryaka, A. V.; Stepanov, S. I.; Medvedev, O. S.; Shapenkov, S. V.; Ubyivovk, E. V.; Vyvenko, O. F. HVPE growth of α-and ϵ-Ga_2O_3 on Patterned sapphire substrates. J. Phys. Conf. Ser. 2019, 1400 (5), 055049.

17. Leach, J. H.; Udwary, K.; Rumsey, J.; Dodson, G.; Splawn, H.; Evans, K. R. Halide vapor phase epitaxial growth of β -Ga_2O_3 and α -Ga_2O_3 films. APL Mater. 2019, 7 (2), 1-8.

18. Nepal, N.; Scott Katzer, D.; Meyer, D. J. MBE growth and characterization of gallium oxide. Gallium oxide Technology, Devices and applications Metal oxides, Elsevier Inc., 2019; 31-46.

19. Ha, M.-T.; Kim, K.-H.; Kwon, Y.-J.; Kim, C.-J.; Jeong, S.-M.; Bae, S.-Y. Understanding thickness uniformity of Ga_2O_3 thin films grown by mist chemical vapor deposition. ECS J. Solid State Sci. Technol. 2019, 8 (7), Q3206-Q3212.

20. Pearton, S. J.; Yang, J.; Cary, P. H.; Ren, F.; Kim, J.; Tadjer, M. J.; Mastro, M. A. A review of Ga_2O_3 materials, processing, and devices. Appl. Phys. Rev. 2018, 5 (1), 011301.

21. Wu, C.; Guo, D. Y.; Zhang, L. Y.; Li, P. G.; Zhang, F. B.; Tan, C. K.; Wang, S. L.; Liu, A. P.; Wu, F. M.; Tang, W. H. Systematic investigation of the growth kinetics of β-Ga_2O_3 epilayer by plasma enhanced chemical vapor deposition. Appl. Phys. Lett. 2020, 116 (7), 072102.

22. Hadamek, T.; Posadas, A. B.; Al-Quaiti, F.; Smith, D. J.; McCartney, M. R.; Demkov, A. A. β-Ga_2O_3 on Si (001) Grown by plasma-assisted MBE with γ-Al_2O_3 (111) Buffer Layer: Structural Characterization. AIP Adv. IP Advances, 2021, 11, 045209.

23. Uno, K.; Ohta, M.; Tanaka, I. Growth mechanism of α-Ga_2O_3 on a sapphire substrate by mist chemical vapor deposition using acetylacetonated gallium source solutions. Appl. Phys. Lett. 2020, 117 (5).

24. Nishinaka, H.; Nagaoka, T.; Kajita, Y.; Yoshimoto, M. Rapid homoepitaxial growth of (010) β-Ga_2O_3 thin films via mist chemical vapor deposition. Mater. Sci. Semicond. Process. 2021, 128, 105732.

25. Pozina, G.; Hsu, C. W.; Abrikossova, N.; Kaliteevski, M. A.; Hemmingsson, C. Development of β-Ga_2O_3 layers growth on sapphire substrates employing modeling of precursors ratio in halide vapor phase epitaxy reactor. Sci. Rep. 2020, 10 (1), 1-9.

26. Moser, N.; Liddy, K.; Islam, A.; Miller, N.; Leedy, K.; Asel, T.; Mou, S.; Green, A.; Chabak, K. Toward high voltage radio frequency devices in β-Ga$_2$O$_3$. Appl. Phys. Lett. 2020, 117 (24), 242101.

27. Bhattacharyya, A.; Ranga, P.; Saleh, M.; Roy, S.; Scarpulla, M. A.; Lynn, K. G.; Krishnamoorthy, S. Schottky barrier height engineering in β-Ga$_2$O$_3$ using SiO$_2$ interlayer dielectric. IEEE J. Electron Devices Soc. 2020, 8, 286-294.

28. Chatterjee, B.; Zeng, K.; Nordquist, C. D.; Singisetti, U.; Choi, S. Device-level thermal management of gallium oxide field-effect transistors. IEEE Trans. Compon. Packag. Manuf. Technol. 2019, 9 (12), 2352-2365.

29. Farzana, E.; Zhang, Z.; Paul, P. K.; Arehart, A. R.; Ringel, S. A. Influence of metal choice on (010) β-Ga$_2$O$_3$ Schottky diode properties. Appl. Phys. Lett. 2017, 110 (20), 202102.

30. Chabak, K. D.; Walker, D. E.; Green, A. J.; Crespo, A.; Lindquist, M.; Leedy, K.; Tetlak, S.; Gilbert, R.; Moser, N. A.; Jessen, G. Sub-micron gallium oxide radio frequency field-effect transistors. IEEE MTT-S Int. Microw. Work. Ser. Adv. Mater. Process. RF THz Appl. IMWS-AMP 2018 2018, 1-3.

31. Hsieh, Y. S.; Li, C. Y.; Lin, C. M.; Wang, N. F.; Li, J. V.; Houng, M. P. Investigation of metal-insulator-semiconductor diode with α-Ga$_2$O$_3$ insulating layer by liquid phase deposition. Thin Solid Films 2019, 685, 414-419.

32. Hu, Z.; Zhou, H.; Feng, Q.; Zhang, J.; Zhang, C.; Dang, K.; Cai, Y.; Feng, Z.; Gao, Y.; Kang, X.; Hao, Y. Field-plated lateral β-Ga$_2$O$_3$ Schottky barrier diode with high reverse blocking voltage of more than 3 kV and high DC power figure-of-merit of 500 MW/cm^2. IEEE Electron Device Lett. 2018, 39(10), 1564-1567.

33. Li, W.; Hu, Z.; Nomoto, K.; Zhang, Z.; Hsu, J. Y.; Thieu, Q. T.; Sasaki, K.; Kuramata, A.; Jena, D.; Xing, H. G. 1230 V β-Ga$_2$O$_3$ Trench schottky barrier diodes with an ultra-low leakage current of <1 μA/cm^2. Appl. Phys. Lett. 2018, 113 (20), 3-7.

34. Qin, Y.; Li, L.; Zhao, X.; Tompa, G. S.; Dong, H.; Jian, G.; He, Q.; Tan, P.; Hou, X.; Zhang, Z.; Yu, S.; Sun, H.; Xu, G.; Miao, X.; Xue, K.; Long, S.; Liu, M. Metal-semiconductor-metal ε-Ga$_2$O$_3$ solar-blind photodetectors with a record-high responsivity rejection ratio and their gain mechanism. ACS Photonics 2020, 7 (3), 812-820.

35. , J.; Hasan, M. N.; Swinnich, E.; Tang, Z.; Shin, S. H.; Kim, M.; Zhang, P.; Seo, J. H. Flexible Crystalline β-Ga$_2$O$_3$ solar-Blind Photodetectors. J. Mater. Chem. C 2020, 8 (42), 14732-14739.

36. Harada, T.; Tsukazaki, A. Control of Schottky barrier height in Metal/β-Ga$_2$O$_3$ junctions by insertion of PdCoO$_2$ Layers. APL Mater. 2020, 8 (4), 041109.

37. Malakoutian, M.; Song, Y.; Yuan, C.; Ren, C.; Lundh, J. S.; Lavelle, R. M.; Brown, J. E.; Snyder, D. W.; Graham, S.; Choi, S.; Chowdhury, S. Polycrystalline diamond growth on β-Ga$_2$O$_3$ for thermal management. Appl. Phys. Express 2021, 14 (5), 055502.

38. Venkata Krishna Rao, R.; Ranade, A. K.; Desai, P.; Kalita, G.; Suzuki, H.; Hayashi, Y. Temperature-dependent device properties of γ-CuI and β-Ga$_2$O$_3$ heterojunctions. SN Appl. Sci. 2021, 3 (10), 796.

39. Kalita, G.; Mahyavanshi, R. D.; Desai, P.; Ranade, A. K.; Kondo, M.; Dewa, T.; Tanemura, M., Photovoltaic action in graphene-Ga$_2$O$_3$ heterojunction with deep-ultraviolet irradiation, Phys. Status Solidi RRL, 2018, 12, 8, 1800198.

40. Kim, J.; Mastro, M. A.; Tadjer, M. J.; Kim, J. Quasi-two-dimensional h-BN/β-Ga$_2$O$_3$ heterostructure metal-insulator-semiconductor field-effect transistor. ACS Appl. Mater. Interfaces 2017, 9 (25), 21322-21327.

41. Sharma, S.; Kalita, G.; Vishwakarma, R.; Zulkifli, Z.; Tanemura, M. Opening of triangular hole in triangular-shaped chemical vapor deposited hexagonal boron nitride crystal. Sci. Rep. 2015, 5, 1-9.

42. Sharma, K. P.; Sharma, S.; Khaniya Sharma, A.; Paudel Jaisi, B.; Kalita, G.; Tanemura, M. Edge controlled growth of hexagonal boron nitride crystals on copper foil by atmospheric pressure chemical vapor deposition. CrystEngComm 2018, 20 (5), 550-555.

43. Rosmi; M. S., Shinde; S. M., Rahman; N. D. A., Thangaraja; A., Sharma; S., Sharma; K. P., Yaakob; Y, Vishwakarma; R. K., Bakar; S. A., Kalita; G., Ohtani; H., Tanemura; M. Synthesis of uniform monolayer graphene on re-solidified copper from waste chicken fat by low pressure chemical vapor deposition, Mater. Resear. Bull. 2016, 83, 573-580

44. Guo, D.; Liu, H.; Li, P.; Wu, Z. W.; S.; Cui, C.; Li, C.; Tang, W. Zero-power-consumption solar-blind photodetector zero-power-consumption solar-blind photodetector based on β-Ga_2O_3/NSTO heterojunction. ACS Appl. Mater. Interfaces 2016, 9 (2), 1619-1628.

CHAPTER 5

5. Conclusion and Future scope of research

Wide bandgap and ultrawide bandgap semiconductors like temperature-dependent device characteristics of the p-type γ-copper iodide (γ-CuI)/n-type β-gallium oxide (β-Ga$_2$O$_3$) attractive candidates for UV and deep UV photodetector application. In this research work, integration of γ-CuI and (β-Ga$_2$O$_3$) heterojunctions with 2-dimensional hBN, and novel inorganic wide bandgap semiconductor, i.e., CuI, is studied. Further, the device performance of Ni/hBN/Ga2O3/In is evaluated with respect to interfacial impurities under UV light illumination.

Chapter 1 The ·fullerene nano cylindrical tubes (FNCT) are introduced in the chapter. The FNCT's were synthesized by a liquid-liquid interface precipitation (LLIP) method is a simple and economically viable approach for directly growing fullerene nanotubes that can be achieved at room temperature with high stability for long periods with semiconducting properties. At the end of this chapter, we discussed the motivation behind the present work.

Chapter 2 Self-assembled nanostructures show electron-transfer improvements when compared with planar electron acceptors. This property allows the development of organic electron devices (e.g., field-effect transistors and solar cells) and optoelectronic devices. Nanotechnology is an emerging field of growing importance. In recent advances in photocatalysts modified with fullerene and its derivatives are overviewed. Exclusive properties and photocatalytic mechanisms of fullerene and its derivatives. The main synthesis strategies and affecting factors are discussed. Excellent photocatalytic applications of photocatalysts modified with fullerene and its derivatives. Challenges and directions on the future design, synthesis, and applications towards the semiconductor materials in various fields.

Chapter 3

Introduce an interesting ultra-wide bandgap semiconductor i.e., β-Ga$_2$O$_3$- gallium oxide Temperature-dependent studies of Ga$_2$O$_3$-based heterojunction devices are important in understanding its carrier transport mechanism, junction barrier potential, and stability at higher temperatures. The fabricated γ-CuI/β-Ga$_2$O$_3$ heterojunction showed excellent diode characteristics with a high rectification ratio and low reverse saturation current at 298 K in the presence of a large barrier height (0.632 eV). The temperature-dependent device characteristics were studied in the temperature range 273 – 473 K to investigate the heterojunction interface. Interestingly with increasing the temperature, a gradual decrease in the ideality factor, and an increase in the barrier height was observed, indicating barrier inhomogeneity at the heterojunction interface.

Chapter 4. introduces one more interesting material hBN (hexagonal boron nitrate) further one more interesting material hBN. In this chapter, a brief introduction of nickel (Ni)-gallium oxide (Ga$_2$O$_3$) Schottky junction with the interfacial hexagonal boron nitride (hBN) layer. The vertical Schottky junction was fabricated with the configuration of Ni/hBN/Ga$_2$O$_3$/In along with its structure, optical and electronic properties is discussed along with its potential application. The turn-on voltage for the forward current of the Schottky junction was significantly enhanced with the hBN interfacial film. Further, the Schottky junction was analyzed under the illumination of deep ultraviolet light (254 nm), obtaining a photoresponsivity of 95.11 mA/W under an applied bias voltage (-8 V). The interfacial layer of hBN for the Ga$_2$O$_3$-based Schottky junction can be significant as a barrier layer to control the turn. In this research work, the materials fullerene, gallium oxide semiconductors have emerged as promising candidates for excellent candidates for potential application in UV photosensor applications by integration with γ-CuI/β-Ga$_2$O$_3$ to form Schottky and p-n heterojunction, respectively. This has opened entirely new possibilities and has

more questions to achieve better performance of the UV photoresponsive devices. Similar to Ni/hBN/Ga$_2$O$_3$/In, various unexplored inorganic semiconductors can be researched to integrate with γ-CuI/β-Ga$_2$O$_3$, and Ni/hBN/Ga$_2$O$_3$/In fabricate p-n heterojunctions to evaluate the device performance and reduce the cost of fabrication on voltage as well as optimizing the device properties for deep UV photosensor applications.

5.1 Conclusion

In this research work, gallium oxide semiconductors have emerged as promising candidates for deep UV photosensor application β-Ga$_2$O$_3$ can form Schottky and p-n junction by integrating with nickel and γ-CuI. We have reported on temperature-dependent ideality factor and barrier height which indicates heterojunction interface inhomogeneity in the fabricated γ-CuI/β-Ga$_2$O$_3$ p-n heterojunction. We fabricated Ni/hBN/Ga$_2$O$_3$/In were in the role of hBN interfacial layer was evaluated furthermore we fabricate heterojunction and evaluated the role of interfacial hBN layer on its device performance and significantly improve device performance wherein UV photoresponsive was observer 95.11mA/W, as well as reduced turn-on voltage, was observed. This study will be useful in fabricating high perforce Ga$_2$O$_3$ based deep UV photo responsive devices.

5.2 Integration of various inorganic semiconductors with γ-CuI/β-Ga$_2$O$_3$ and Ni/hBN/Ga$_2$O$_3$/In

As discussed, integration of γ-CuI/β-Ga$_2$O$_3$ /In it has a unique outcome with excellent UV photoresponsive photo voltage with stable operation at a high temperature of 273 – 473 K. This study can be expanded by integrating γ-CuI/β-Ga$_2$O$_3$ with various other suitable p-type inorganic semiconductors like Bismuth ox iodide (BiOI), which is a p-type semiconductor with a bandgap of ~ 2.0 eV. Currently, BiOI is being widely researched for various electronic applications, and in this light,

integration with Ni/hBN/Ga_2O_3/In could be suitable. Further, the fabricated heterojunctions could be evaluated for high-temperature operations since both γ-CuI/β-Ga_2O_3 possess high-temperature stability. Thus, this could lead to the fabrication of novel Ga_2O_3 based UV and deep UV photodetectors.

Acknowledgements

My deepest gratitude goes to my supervisor **Prof. Yasuhiko Hayashi** for providing an opportunity to research under his kind guidance. He offered me so much advice, patiently supervised me, and guided me in the right direction. I've learned a lot from him; I could not have completed my dissertation without his guidance. It was an honor to be his student. I will always be indebted to him.

My deep gratitude to **Assoc. Prof. Kazuhiro** and **Assoc. Prof. Yoshifumi Yamashita** for their guidance during my thesis correction with encouragement, and valuable suggestions. I appreciate his kind support and help.

I want to thank **Associate Takeshi Nishikawa** for his kind support.

I am also pleased to say Thank you to **Dr. Hiroo Suzuki** for his insightful comments and encouragement during my PhD work.

Thank you fully for being good friends around me to support me during my PhD life and stay at Okayama. **Mr. Abhinav, Dr. Mandeep Singh, Mr. Sai Krishna, Mr. Susumu Yamamoto and Ms. Mitsuhata.**

I sincerely extend my heartful thank you to **Prof. Golap Kalita**, (Nagoya institute of science and technology, Nagoya), who provided me with great advice, comments, and discussions during my PhD work. Thank you so much for guiding me in my research endeavors and writing this thesis

I am so thankful to my lab colleagues at Nagoya institute of science and Technology, **Dr. Ajinkya Ranade** and **Dr. Pradeep Desai**, who helped me right from the beginning. Also, I would like to thank my other lab mates and friends, **Miss. Bhagyashree Todankar**, **Mr. Shuhei**, **Mr. Kai Okazai, Mr. Venky, Dr. Rama, Dr. Mallareddy, Dr. Satish, Mr. Rahul, Mr. Arjith, Miss. Nishtha,** for their support during my stay at Nagoya.

List of research achievements

I. Papers published related to present work

1. **Rama Venkata Krishna Rao,** ..; Karthik, P. S.; Abhinav, V. K.; Lin, Z.; Myint, M. T. Z.; Nishikawa,T.; Hada, M.; Yamashit, Y.; Hayashi, Y.; Singh, S.P "**Self-assembled C$_{60}$ fullerene cylindrical nanotubes by LLIP method**" *IEEE Xplore,,*August 22, (2016). Article DOI: 10.1109/NANO.2016.7751386.

2. **Rama Venkata Krishna Rao**, Ajinkya K. Ranade, Pradeep Desai, Golap Kalita, Hiroo Suzuki & Yasuhiko Hayashi, "**Temperature-dependent device properties of γ-CuI and β-Ga$_2$O$_3$ heterojunctions**" *Springer - SN Applied Science*, (2021). **Article DOI:** 10.1007/s42452-021-04774-3

3. **Rama Venkata Krishna Rao ,** Ajinkya K. Ranade, Pradeep Desai, Bhagyashri Todankar, Golap Kalita, Hiroo Suzuki1, Masaki Tanemura, Yasuhiko Hayashi, "**Characteristics of vertical Ga2O3 Schottky junctions with interfacial hexagonal boron nitride film**" *ACS Applied Electronic Materials.* **Date of Acceptance:** Under Communication.

II. Other Publications:

4. Karthik, P.; Shimo, Y.; Lin, Z.; **Rama Venkata Krishna Rao;** Gong, X.; Yoshida, M.; Hada, M.; Nishikawa, T.; Hayashi, Y.; Singh, S. P." **Carbon Nanostructures Synthesized via Self-Assembly (LLIP) and Its Application in FET.**" *IEEE 11th Annual International Conference on Nano/Micro Engineered and Molecular Systems (NEMS)* 2016.

List of Oral Presentations

1. **<u>Rama Venkata Krishna Rao</u>**, Ajinkya K. Ranade, Pradeep Desai, Golap Kalita, Hiroo Suzuki & Yasuhiko Hayashi, "**Temperature-dependent device properties of γ-CuI and β-Ga2O3 heterojunctions**" ISAJ (*Indian Scientists Association In japan*) 2020 Tokyo.